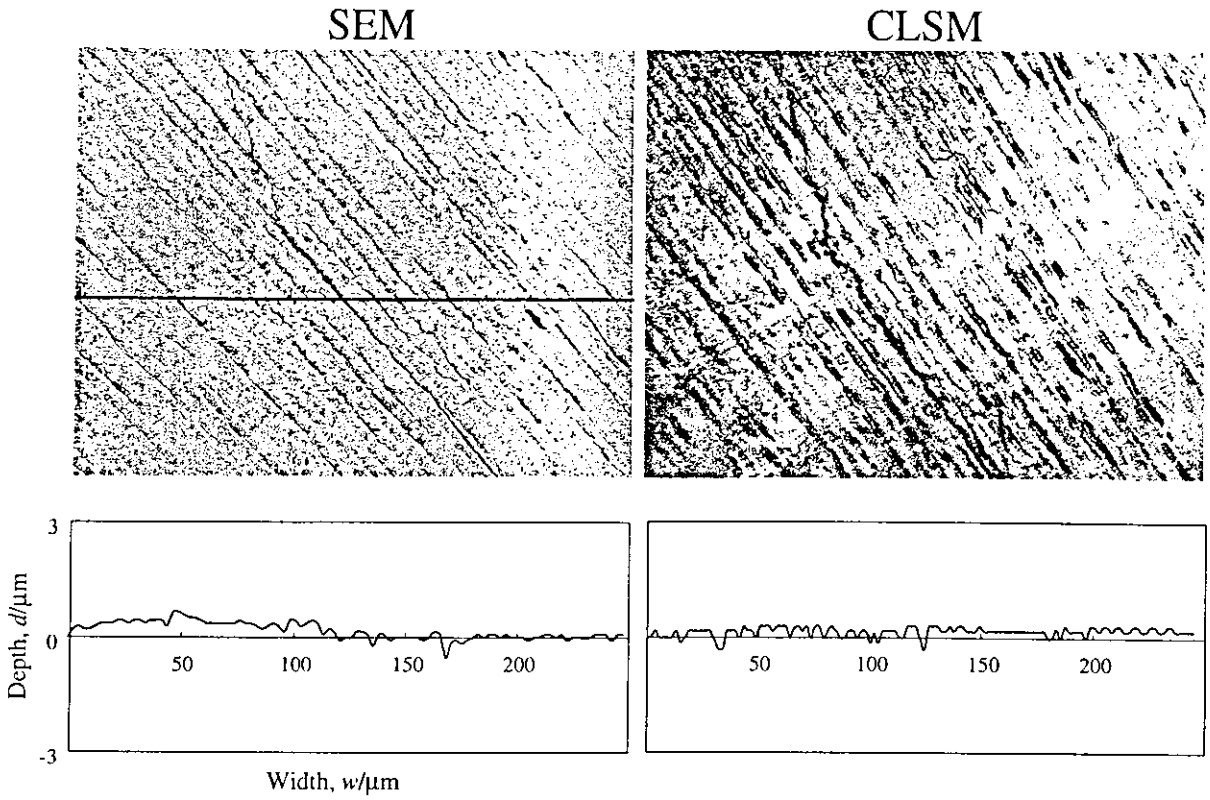

Fig. 4 SEM and CLSM images and their respective profiles of laser-irradiated dentin obtained from the same area of the same specimen. The images are enlargements of the areas delimited in Fig. 2.

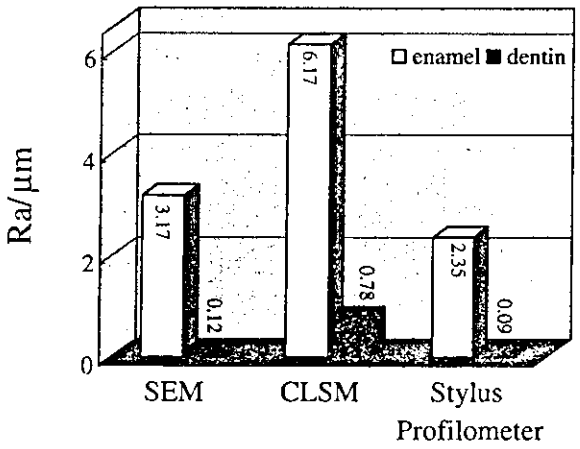

Fig. 5 Comparison of SEM, CLSM and conventional stylus profilometer measurement of surface roughness values (*Ra*) on enamel and dentin.

for enamel and 0.09 μm for dentin.

The *Ra* results obtained with the SEM and CLSM shown in Figs. 3 and 4 and those for the stylus profilometer are compared in Fig. 5. The figure shows that the order of *Ra* values was the same and that there were differences of 1.95- to 6.5-fold in factors between the SEM and CLSM. The values obtained with the SEM were generally smaller than those for the CLSM, but larger than with the stylus profilometer. Dentin had a lower *Ra* than enamel.

Figure 6 shows a further enlarged SEM image (a), 3D image (b) and depth profile (c) of laser-irradiated enamel. The depth profiles were obtained from the line shown in (a). The dashed circle (a) shows the basic structural unit of the enamel prism, which is also called the enamel rod. Each prism is divided into a head and tail and is constituted of a large numbers of hydroxyapatite crystallites. These crystallites run parallel along the long axis of the prism at the head, and diverge gradually from this to become angled 65–70° to the long axis at the tail. In the tail of the enamel prism shown by the dashed circle, the crystallites diverge laterally forming a flame shape and in the center the crystallite ends appear on the surface. Regions with crystallites non-parallel to the irradiated surface remains, while the adjacent areas with the crystallites parallel to the surface have flaked off. The depth profile (c) shows that the size of the areas where material is removed was about 5 μm, corresponding to the size of the enamel prism. The grooves formed conferred roughness of 0.4 μm. The three-dimensional image (b) can represent the surface morphology viewed from any desired angle. In this case it is the upper left.

Figure 7 shows the SEM image of Fig. 2(a), 3D image (b) and depth profile (c) of laser-irradiated dentin at higher magnification (×5000). Cracks were observed mostly inside the peritubular dentin where the contrast was brighter than for intertubular dentin. It was known from the CLSM image (Fig. 4) that dentinal tubules lay below the peritubular dentin by comparison with the SEM image. The surface roughness was 0.17 μm.

Figure 8 shows the Raman spectra of non-irradiated (a) and irradiated (b) dentin. Phosphate vibrations in hydroxyapatite are shown at ν_2 (350–500 cm^{-1}), ν_4 (550–650 cm^{-1}), ν_1

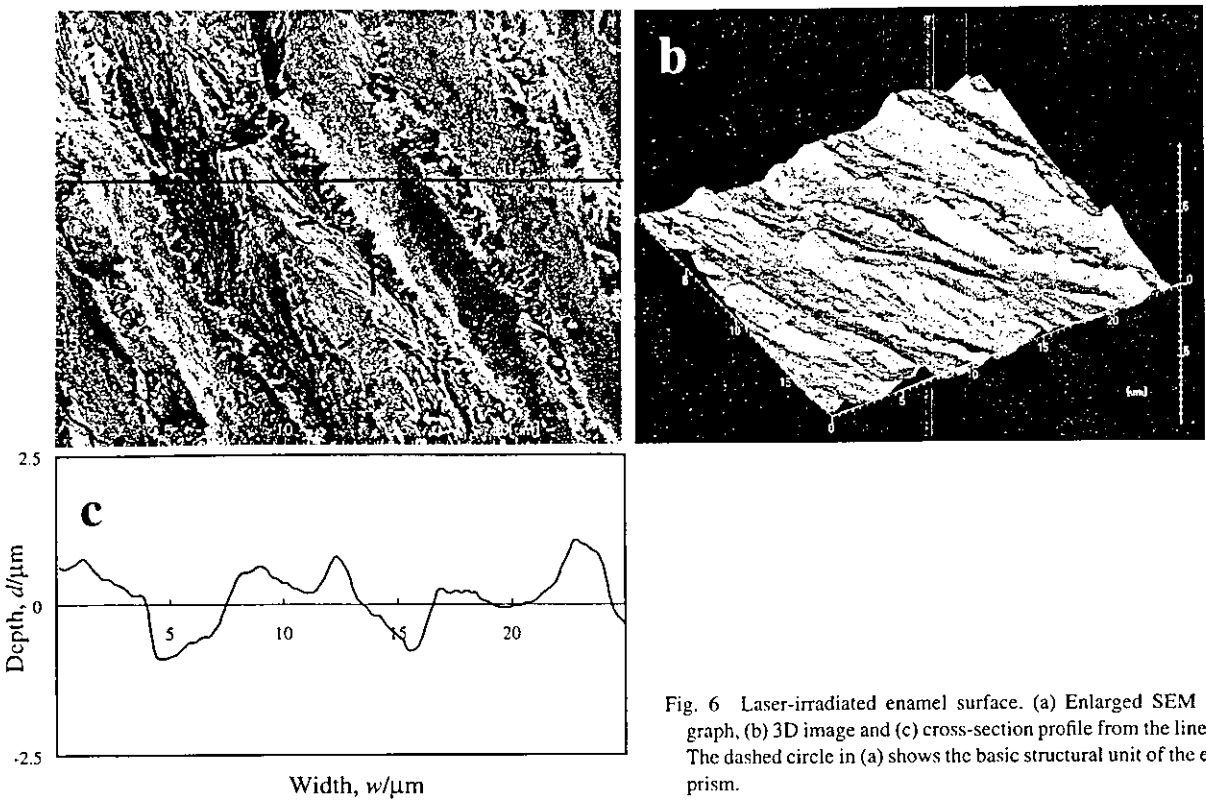

Fig. 6 Laser-irradiated enamel surface. (a) Enlarged SEM photograph, (b) 3D image and (c) cross-section profile from the line in (a). The dashed circle in (a) shows the basic structural unit of the enamel prism.

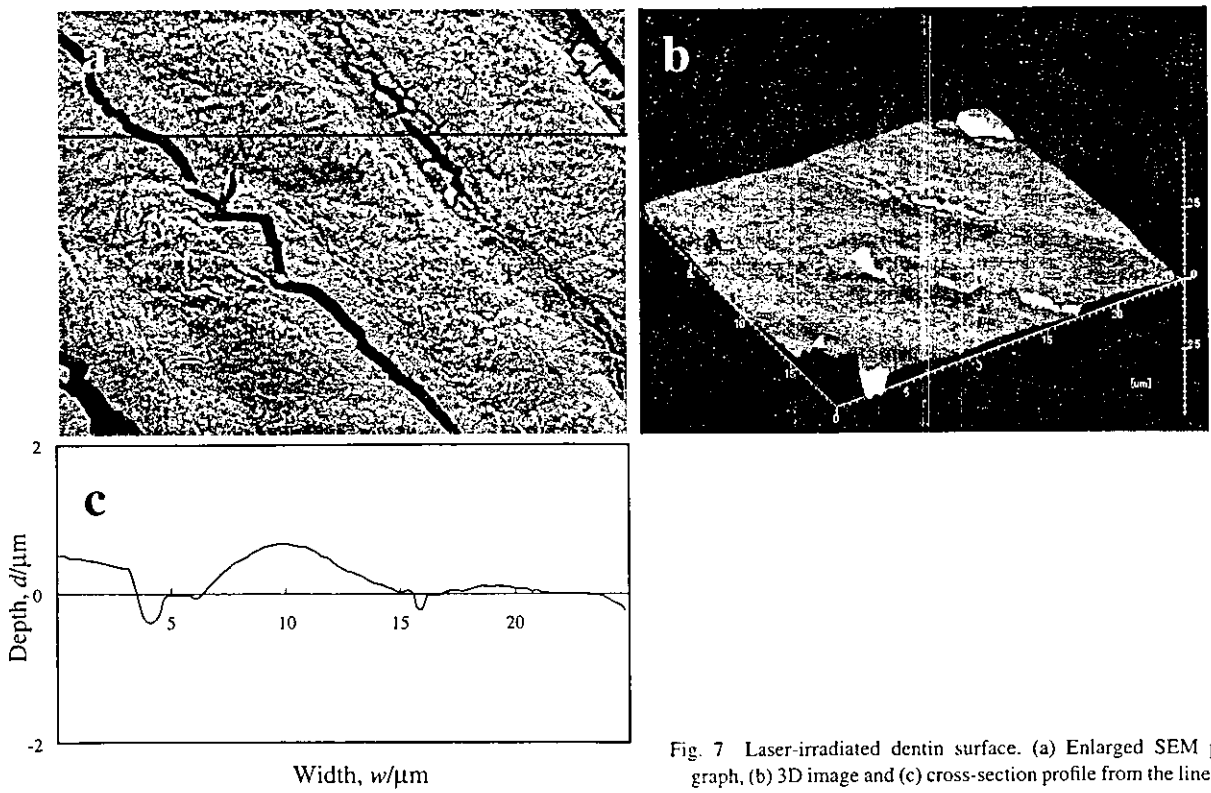

Fig. 7 Laser-irradiated dentin surface. (a) Enlarged SEM photograph, (b) 3D image and (c) cross-section profile from the line in (a).

(900–1000 cm^{-1}) and ν_3 (1000–1130 cm^{-1}). The organic collagen matrix peaks appear at 1257, 1470, 1661 and 2945 cm^{-1} (Fig. 8a). After irradiation, these peaks were lost and broad peaks due to amorphous carbon were observed in the range of 1346–1580 cm^{-1} (Fig. 8b). The background intensity became higher. Laser-irradiated enamel also showed a higher background intensity than non-irradiated enamel. However, the change of enamel was smaller than for dentin. The ν_2, ν_4, ν_1 and ν_3 bands were observed after CO_2 laser irradiation, although less intensely.

To observe the effect of laser-irradiated collagen on dentin, treatment with 35% phosphoric acid was done and the

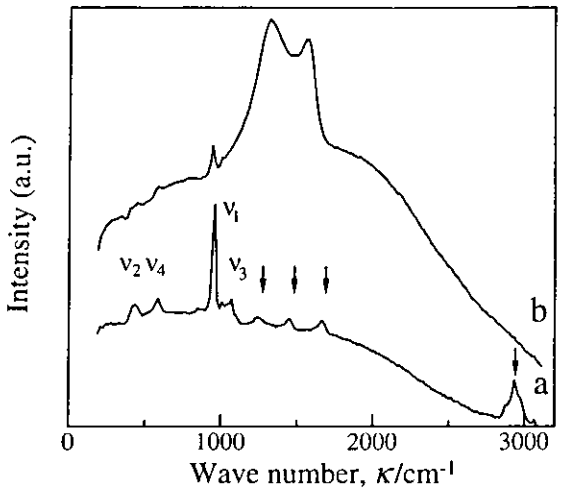

Fig. 8 Raman spectra of dentin before (a) and after irradiation (b). The ν_1–ν_4 peaks are attributed to phosphate and arrows to collagen.

exposed collagen fibrils were irradiated with the laser. Figure 9 shows SEM images of non-etched (a) and acid-etched (b) dentin after laser irradiation. Non-etched lased dentin changed to a slightly white contrast in the SEM image. The morphology of irradiated and non-irradiated areas was not much different (a). On the other hand, the lining of dentinal tubules on acid-etched laser-irradiated dentin looked more markedly white (b). Outside of the irradiated area, a band of melted material was observed (arrows).

Figure 10 shows SEM micrographs of non-etched and acid-etched dentin before (a) and after (b) laser irradiation at higher magnification. Non-etched dentin did not show much change in structure after laser irradiation (b). Cracks were observed on some parts of peritubular dentin. After acid etching, the exposed collagen fibrils were apparent on dentin (a). These collagen fibrils disappeared with application of the laser and melted hydroxyapatite was observed (b).

4. Discussion

4.1 Imaging and depth-profile analysis of teeth irradiated by the CO_2 laser

The SEM (BSE) and CLSM had different contrast levels. Groove-surface images such as those observed on enamel after laser irradiation gave rise to strong contrast with the CLSM, emphasizing the irregular surface (Fig. 3). The inside under the surface could also be viewed with limited depth as observed for dentinal tubules in Fig. 4. Correlating the *Ra* results for the SEM and CLSM, it was observed that the CLSM tended to produce larger values. This may be explained by the difference between the scanning methods. The image of the SEM is formed with the numbers of electrons reflected from the surface while the CLSM obtained the images from a series of optically sliced sections parallel to the tooth surface. The lower resolution of about 0.1 μm limited by the light wavelength and the optically sectioned slice thickness reasonably set to 0.5 μm (Z-interval) in CLSM may limit the mechanical scanning. Although there are other methods to improve the value of the resolution, a resolution of around 0.5 μm may limit the detection of roughness less than that.

The conventional, contact stylus profilometer was employed using the same scanning line 250 μm in length as obtained from SEM and CLSM for comparison. However, the selection of the same area was approximate and precise selection was difficult. Using the stylus profilometer, the results for *Ra* did not provide much detail of the surface compared to the SEM and CLSM. The *Ra* was the lowest, probably due to the limitation of the stylus profilometer tip.

The CLSM provides subsurface examination of intact tooth samples,[3] which have transparency to some extent, offering additional data to those obtained by conventional

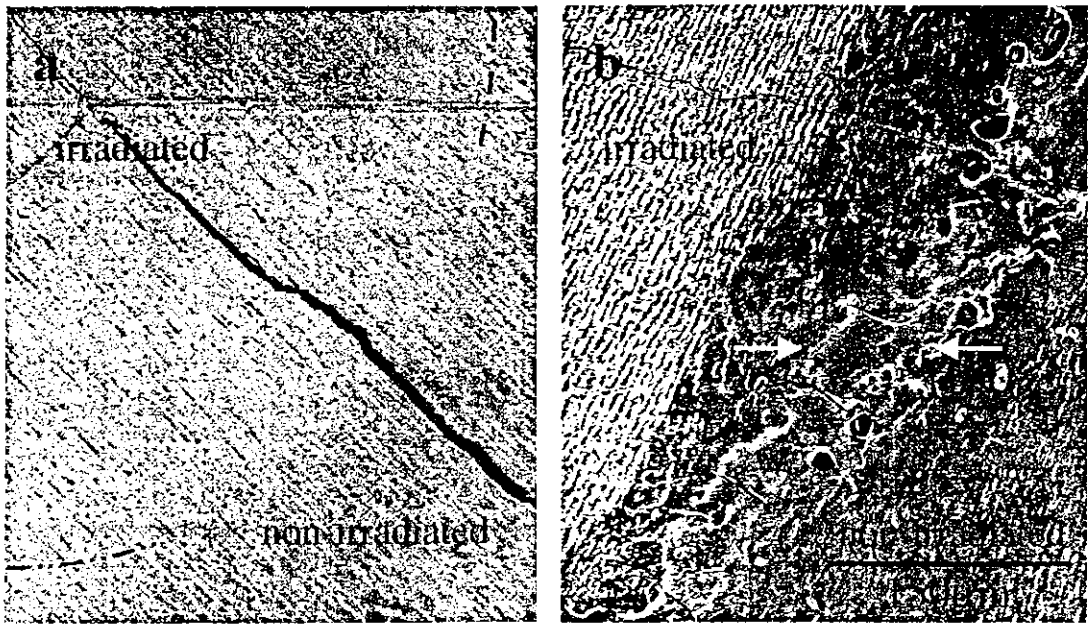

Fig. 9 Comparison of laser irradiation effect of non-etched (a) and acid-etched (b) dentin by SEM. The stippled line in (a) shows the boundary between irradiated and non-irradiated areas.

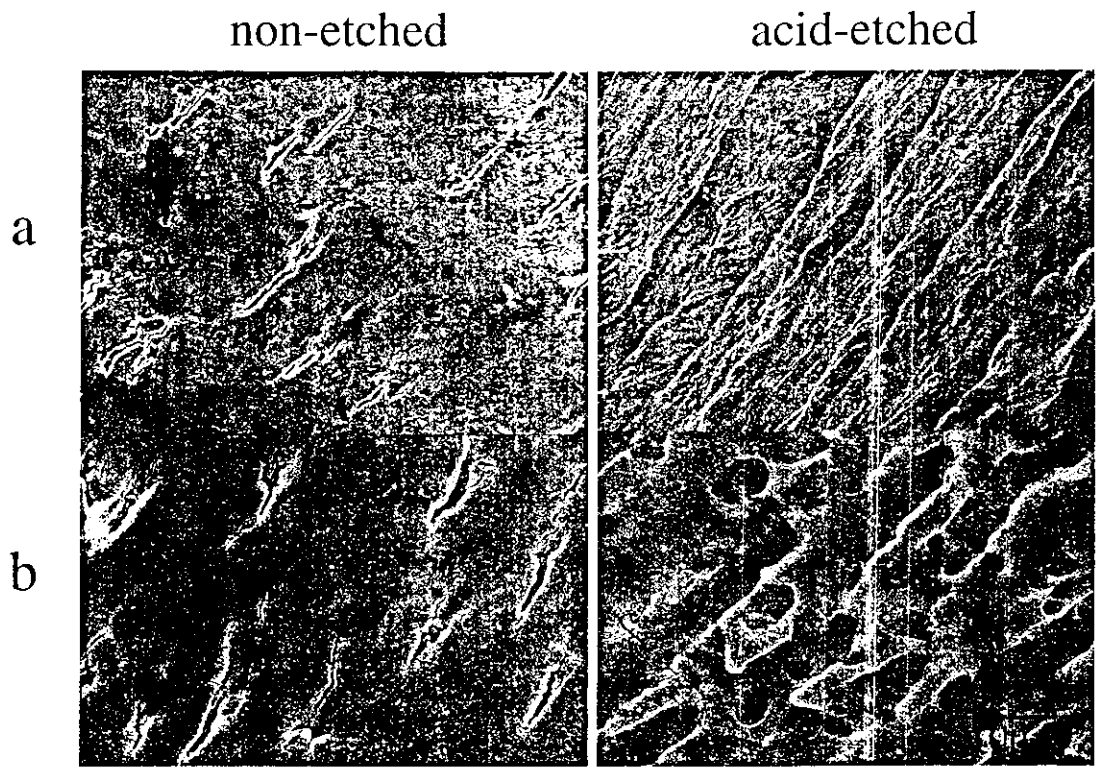

Fig. 10 SEM micrographs of non-etched and acid-etched dentin before (a) and after (b) laser irradiation at high magnification.

methods such as the SEM. Although there are advantages regarding the CLSM technique such as the capacity of determine the depth profile analysis from 3D reconstructions of the cavity shape and cross sections without the need for sample cutting,[8] Watson warned against using 3D reconstruction made from serial optical sections due to the low resolution in the optical axis of the microscope that could cause deformation in the image.[9] On the other hand, the SEM's higher resolution results in well-defined detailed images, especially at higher magnifications. SEM 3D images also offer details of tooth surface morphology and roughness after laser irradiation, which makes it possible to construct images observed from any angle.

The conventional stylus profilometer is useful for analysis of large areas, but the selection of desired area on a microscale is not possible. The topographic SEM and CLSM provide quantitative surface analysis from the microarea correspondent to a microscopic image for a delicate surface like the tooth via a non-contact method.

4.2 Raman spectra

The background intensity of Raman spectra on dentin became higher after laser irradiation. It is known that this, mostly contributed by fluorescence, is lower as the binding is tighter.[10] Therefore, the high background intensity in the laser-irradiated surface suggests breakage of the cross-linking in the structure. Bands attributed to the organic collagen matrix observed at 1257, 1470, 1661 and 2945 cm^{-1} disappeared after CO_2 laser irradiation and peaks attributed to amorphous carbon appeared instead in the range of 1346–1580 cm^{-1} (Fig. 8b). This finding suggests that laser irradiation instantly heats the tooth surface to a high temperature, resulting in the burning and decomposition of collagen and formation of amorphous carbon. Enamel showed small changes compared to dentin. This is due to the differences in morphological structures and physical properties of the dental hard tissues. Enamel is composed mostly of inorganic material (hydroxyapatite) with no collagen. The higher background intensity observed after laser irradiation of enamel showed that the hydroxyapatite structure was partly decomposed.

4.3 Effects of CO_2 laser irradiation on enamel and dentin

The absorption of laser light in dental hard tissue is important for the ablation of teeth[11] and is very much dependent on the wavelength of the laser light.[12] Dental hard tissue has absorption bands ranging from 9.0 to 11.0 μm. Therefore, a CO_2 laser with a wavelength of 10.6 μm has strong absorption in enamel and dentin. Although CO_2 laser has a high absorption rate by water (Absorption Coefficient, AC = 10^3), the absorption of hydroxyapatite is higher, resulting in an increase in temperature.[13] Thus, thermal shock may cause cracks in the tooth.

Besides the influence of the laser wavelength, power, pulse duration, number of pulses and spot size in the radiation effect, the absorption of laser light also depends on the nature of the biological tissue. Enamel is a highly mineralized tissue composed of 96% inorganic material (hydroxyapatite crystallites), 1% organic material and 3% water. Although enamel has a low tensile strength and is brittle, its rigidity and the flexible support of the underlying dentin minimize the possibility of fracture. Dentin is composed by 70% inorganic material, 20% organic material and 10% water. The

content of the fibrous protein collagen, the main component of the organic material, is much higher than in enamel. This may explain the carbonization of dentin.

3D-SEM observation of laser-irradiated enamel at high magnification (Fig. 6) showed that the laser had a tendency to detach material in the head of the enamel prism where crystallites ran parallel to the long axis of the prism. CO_2 laser-induced surface alteration depends on the prism orientation, and consequently, on the orientation of the hydroxyapatite crystallites. Ferreira *et al.* also found flaked-off material to be more common in parallel than in perpendicular prism orientation to the specimen surface.[14] It was suggested that the cracks formed due to the thermal shock parallel to the irradiated enamel, if allowed to propagate along the lines of weakness between prisms and crystals, would cause flaking off or ejection of material. On the other hand, when crystals are in transverse orientation in the irradiated surface such as those observed in the dashed circle in Fig. 6, the lines of weakness would generally lie perpendicular to the irradiated surface. This would impede the propagation of cracks and hence partially inhibit the ejection of material. On dentin, cracks were induced inside the peritubular dentin (Fig. 7). The content of hydroxyapatite in this area is higher than in intertubular dentin. Thus, the structure is brittle and more susceptible to crack formation by thermal shock.

4.3.1 Effect of acid etching prior to laser irradiation

In Fig. 9 the difference of contrast between non-etched and acid-etched dentin after laser irradiation can be seen. The laser-irradiated area became white. This contrast change was stronger on acid-etched dentin. This suggested that the average atomic numbers of inorganic and organic components were higher in the irradiated area than in non-irradiated, and more marked in acid-treated dentin. This is in accordance with the fact that hydroxyapatite is formed by heavier atoms (Ca, P), not the light atoms (C, N, O, H) found in collagen. In Fig. 9b, there is a band of melted material around the laser-irradiated area (arrows). One possible explanation for the appearance of this structure is that the explosive pressure caused by the instant heat of laser irradiation may have arrested the melted structure from the center, depositing and consolidating the material in the periphery.

Pretreatment using acid etching much increased the effect of laser irradiation on the structural modification of dentin. The collagen fibrils left after acid etching evaporated and melted hydroxyapatite was observed (Fig. 10). There was not much change on the non-etched dentin after laser irradiation. This may be because in non-etched dentin, the collagen and apatite are mixed. Although the CO_2 laser light is highly absorbed by water, it is much more absorbed by hydroxyapatite. Therefore, the underlying layer of hydroxyapatite left under the collagen fibrils after acid etching may have a tendency to more directly be affected by the laser. Thus, the addition of acid etching pretreatment enhanced the laser effect.

5. Conclusions

(1) The SEM and CLSM provided non-contact profile analysis and the *Ra* of the irradiated tooth surface in selected microareas in a plane with high resolution, which was an additional advantage over the conventional stylus profilometer.

(2) The SEM and CLSM showed inverse contrast and their respective non-contact surface roughness analyses could quantitatively evaluate the surface profile and roughnesses of enamel and dentin after laser irradiation.

(3) Raman spectroscopy suggested that the hydroxyapatite structure was partly decomposed and confirmed the carbonization of collagen in dentin after laser irradiation.

(4) CO_2 laser-induced surface alteration depends on the crystallite orientation of the enamel prism. Regions with crystallites nonparallel to the irradiated surface remained, whereas areas with crystallites parallel to the surface flaked off.

(5) The laser effect on dentin was enhanced by the addition of acid-etching pretreatment. The acid-etched dentin caused the disappearance of fibril collagen and melting of hydroxyapatite, whereas the non-etched surface did not show much change under microscopic analysis, except for some cracks on peritubular dentin.

Acknowledgments

We would like to thank: Dr. Takaki Kumazawa, Dr. Yoji Kamiura and the staff of Kumazawa Dental Clinic for the use of the CO_2 laser; Prof. Minoru Wakita of Hokkaido University for discussions relating to enamel structure; Dr. Yoshinobu Nodasaka and Mr. Toshi Sugawara for their kind help, and Hitachi High-Technologies Corporation for their 3D analysis using SEM.

REFERENCES

1) J. D. Featherstone and D. G. Nelson: Adv. Dent. Res. 1 (1987) 21–26.
2) S. M. McCormack, D. Fried, J. D. Featherstone, R. E. Glena and W. Seka: J. Dent. Res. 74 (1995) 1702–1708.
3) F. Watari: J. Mater. Sci., Materials in Medicine. 12 (2001) 189–194.
4) C. J. Arcoria, M. G. Lippas and B. A. Vitasek: J. Oral Rehabil. 20 (1993) 213–224.
5) B. Al-Nawas, K. A. Grotz, H. Gotz, G. Heinrich, T. G. Rippin, T. E. Stender, H. Duschner and W. Wagner: Scanning. 23 (2001) 227–231.
6) D. R. Radford, T. F. Watson, J. D. Walter and S. J. Challacombe: J. Prosthet Dent. 78 (1997) 200–208.
7) H. Tsuda and J. Arends: Adv. Dent. Res. 11 (1997) 539–547.
8) A. Ebihara, B. Majaron, L. H. Liaw, T. B. Krasieva and P. Wilder-Smith: Lasers Med. Sci. 17 (2002) 198–207.
9) T. F. Watson: Adv. Dent. Res. 11 (1997) 433–441.
10) J. J. Workman: *Hand Book of Organic Compounds*, Vol. 1, (A Harcourt Science and Techonology Co., San Diego, 2001) pp. 339–349.
11) C. J. Whitters and R. Strang: Lasers Surg Med. 26 (2000) 262–269.
12) H. J. Koort and M. Frentzen: *Laser Surgery. Advanced Characterization, Therapeutics and Systems III*, Vol. 1643, ed. by R. R. Anderson and A. Katzir, (SPIE Proc, 1992) pp. 403–411.
13) H. J. Koort and M. Frentzen: *Lasers in Dentistry*, ed. by L. J. Miserendino and R. M. Pick, (Quintessence Publishing Co., 1995) pp. 57–70.
14) J. M. Ferreira, J. Palamara, P. P. Phakey, W. A. Rachinger and H. J. Orams: Arch. Oral. Biol. 34 (1989) 551–562.

Materials Transactions, Vol. 45, No. 4 (2004) pp. 1140 to 1146
Special Issue on Frontiers of Smart Biomaterials
©2004 The Japan Institute of Metals

Laser Welding of Titanium and Dental Precious Alloys

Keiji Iwasaki*, Shoji Ohkawa, Motohiro Uo, Tsukasa Akasaka and Fumio Watari

Dental Materials and Engineering, Department of Oral Health Science, Graduate School of Dental Medicine, Hokkaido University, Sapporo 060-8586, Japan

The performance of laser welding of Ti and two dental precious alloys (Ag-Pd-Au, Au-Pt-Ag) was investigated by mechanical testing and microscopic observation, using butt joint as design. The laser irradiation was done using a commercial Nd:YAG dental laser-welding device in a single pulse mode with output currents 150, 200, 250, 300 A, spot diameters 0.6, 0.9, 1.2 mm, and pulse duration 10 ms. The average welding fracture strength of the dissimilar metals were 108.9 and 137.2 MPa for Ti and Ag-Pd-Au alloy, and Au-Pt-Ag alloy, respectively. The average welding fracture strength of the same metals were 594.9, 648.8 and 312.9 MPa for Ti, Ag-Pd-Au alloy and Au-Pt-Ag alloy. The hardness increased in weld zone, compared with the base metals. Penetration depths were affected by the welding conditions such as the output currents and spot diameters. The welding cracks and porosity were observed in microstructures of the welds. Mapping by EPMA showed the remarkable heterogeneity of the component metals concerned. The welding cracks, porosities and granular precipitates similar to metallic compounds in the weld zones were suggested as the cause for lower welding fracture strength in the dissimilar welds, compared with the similar metals.

(Received December 17, 2003; Accepted March 26, 2004)

Keywords: *laser welding, titanium, dental precious alloys, tensile test, welding strength, electron probe micro analyzer, hardness*

1. Introduction

Gordon and Smith first described the use of laser energy for joining dental casting alloys in 1970.[1] They stated that the laser-welding technique is less time-consuming and produced more accurate and stronger joints for both fixed and removable partial prostheses. Preston and Reisbick[2] compared the ultimate tensile strength of noble base metal, and mixed metal welds to conventional dental joining methods and found that "laser fusion is as good as, or better than, unions created by conventional dental joining methods". Smith *et al.*[3] stated that the laser welding of dental casting gold alloys is "metallurgically feasible" after an investigation of the weld properties and microstructure. The laser welding process was introduced into dentistry at the end of the 1980s. Joining technique of dental appliances was simplified by the development of welding machines. Metal prosthetic pieces are joined directly on a master cast of gypsum without placing in investment. The laser welding has an advantage to heat only limited areas for the bonding as a concentrated laser-light beam is applied. The laser welding is a kind of high-density energy welding and is generally suitable for welding non-precious alloys such as Co-Cr and Ni-Cr.[4]

In recent years titanium and its alloys have been used to produce crowns, bridges, dentures and artificial roots because of their good biocompatibility, and outstanding mechanical properties.[5] In addition, the progress of precise dental casting and joining methods of titanium has accelerated numerous applications development. In the case of ordinary soldering it is very difficult to bond titanium based materials because they are oxidized easily in air at high temperature. In order to solve the problem an infrared heating method was developed using an argon atmosphere and Ti-Ni-Cu solder.[6–8] Laser welding of titanium with the dental casting has been also studied.[9–12] Laser welding is effective for joining titanium because the procedure is easier than the dental soldering. Though the dental casting of titanium is continuously improved, defects are often present in cast titanium. Cast titanium meant to clasp the dentures are liable to break due to the defects. If the cast titanium denture plates can be joined to cast or wrought clasps made of dental precious alloys such as Ag-Pd-Au alloy and Au-Pt-Ag alloy by laser welding, different designs of the dentures would be possible. However, no systematic research was carried out on the laser welding of dissimilar metals like Ti and dental precious alloy.

The commercial dental laser welding device used by us has three operating parameters that can be set: output current, spot diameter and irradiation time. In order to clarify the problems of laser welding of Ti and the dental precious alloys, the objective of this study was to investigate laser welding between Ti and Ag-Pd-Au, Au-Pt-Ag alloys with different operating parameters. The tensile fracture strength, hardness and microstructures of the welds were examined.

2. Materials and Methods

2.1 Preparation of test specimens

Materials used are shown in Table 1. The wrought metal

Table 1 Product Used in the Study.

Base metal	Product	Composition (mass%)	Melting point (°C)	Company
titanium	JIS Type II	<0.015H, <0.20O, <0.05N, <0.25Fe, Bal. ·Ti	1668	Niraco. Co.
Ag-Pd-Au alloy	Aurum Cast 12	45Ag, 20Pd, 20Cu, 12Au, 1Zn, 1In, Ir(0.02)	920~868	Nihonbashi Tokuriki. Co.
Au-Pt-Ag alloy	PC-3	65Au, 12Ag, 10Pt, 10Cu, 2Pd, Ir(0.02)	1020~960	Nihonbashi Tokuriki. Co.

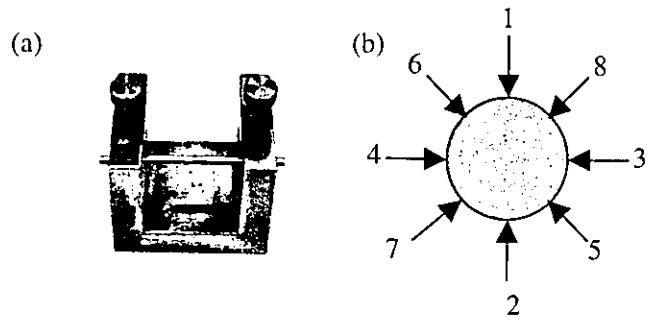

Fig. 1 Preparation of test specimens. (a) Holding jig of test specimen. (b) Direction of laser irradiation.

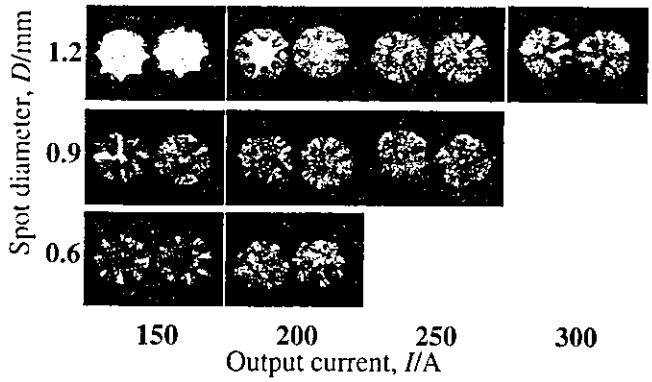

Fig. 2 Fracture surface of welds of titanium and Au-Pt-Ag alloys.

bars have 3.0 mm in diameter and 30 mm in length. The laser welder used for the experiment is the dental laser welder (TLL7000PLUS, ADT, Tokyo, Japan). Weld areas were sandblasted with alumina (50 μm) at 0.2 MPa, and cleaned ultrasonically in detergent solution first then in pure water, and finally degreased with acetone. The bars were fixed in the jig shown in Fig. 1(a). Two pieces of Ti and precious alloy bar were placed in the jig to maintain the alignment of the bar throughout the joining procedures. A pulsed Nd:YAG laser unit was used for the welding operations, which were carried out in an argon atmosphere. The focus of the laser was set at the interface of the two bars. Laser welding shots were carried out on diagonal lines eight times while argon gas was blown as shown in Fig. 1(b). Output currents of the laser were 150, 200, 250 and 300 A. Spot diameters were 0.6, 0.9 and 1.2 mm. The pulse duration was fixedly 10 ms.

2.2 Measurement of fracture strength

The tensile test was carried out using universal test machine (Model 4202, Instron-Japan, Tokyo, Japan) with cross head speed 1 mm/min and a gauge length of 20 mm. The test was done five times for each welding conditions. Cross section areas were calculated using original diameters of the metal bars.

2.3 Observation of fracture surfaces

The fracture surface of tensile specimens was observed macroscopically using a digital microscope (VH-6300, KEYENCE Co. Tokyo, Japan) at magnifications of 25 and details by a scanning electron microscope (S2380N, HITACHI Co. Tokyo, Japan).

2.4 Electron probe microanalyzer

Butt-welded specimens with different conditions were embedded in epoxy-resin using rubber moulds. After the resin set, the embedded specimens were stripped from the moulds. The specimens were ground to the half section to expose the weld zones using 600, 800 and 1000-grit Emery papers and polished by a lapping wheel with suspensions of alumina (2 micron, 1 micron). The polished surfaces were coated by evaporation of carbon for the electric conductivity. Mapping images of Ti, Au, Pt, Pd, Ag and Cu were obtained at the weld zones with an electron probe microanalyzer (EPMA) (JXA-8900, JEOL, Akishima, Japan). At the same time, reflection electron images were observed.

2.5 Hardness test

Welded region hardness was measured by Vickers hardness tester (Type M, Shimadzu, Kyoto, Japan), using the same polished specimens as for the EPMA observation. The measurement area extends 1 mm from the weld on each bar of the joint. The measurements were done with 0.1 mm pitch, along the lines placed at 0, 0.5 and 1.0 mm below the section edge. The load was 200 g and loading times was 15 seconds.

3. Results

The fracture surfaces for Au-Pt-Ag alloy were shown in Fig. 2 for different spot diameters and output currents. The penetration depths reach the core of the bars when the output currents increased and the spot diameter decreased. For too big output currents and too small spot diameters, the metals are volatilized, and the penetration areas consequently decreased. The deep concave surface was formed in the weld zone by sputtering and under-fill for the 0.6 mm spot diameter.

Figure 3 shows the reflection electron micrographs of vertical cross section of the welded zone under the conditions that showed the largest fracture strength for the combinations of Ti and Au-Pt-Pd (a), Ag-Pd-Au alloys (b). In both micrographs, it was observed the contrast differences characteristic to reflection electrons. Centerline cracks and porosities were observed in both welds.

Figure 4 and Fig. 5 show the secondary electron images and elemental mapping images of the welded zones between Ti and Au-Pt-Ag, Ag-Pd-Au alloy, respectively. In the case

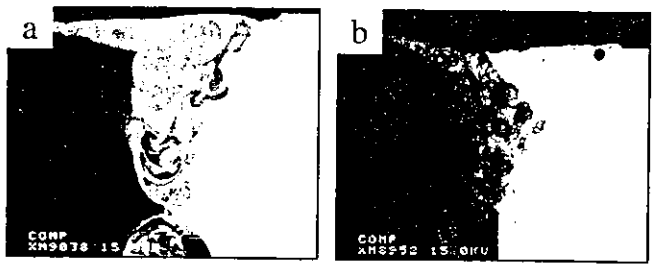

Fig. 3 Reflection electron images of the weld zones. a: Titanium and Au-Pt-Ag alloy. (output current 250 A, spot diameter 1.2 mm, pulse duration 10 ms). b: Titanium and Ag-Pd-Au alloy. (output current 200 A, spot diameter 1.2 mm, pulse duration 10 ms).

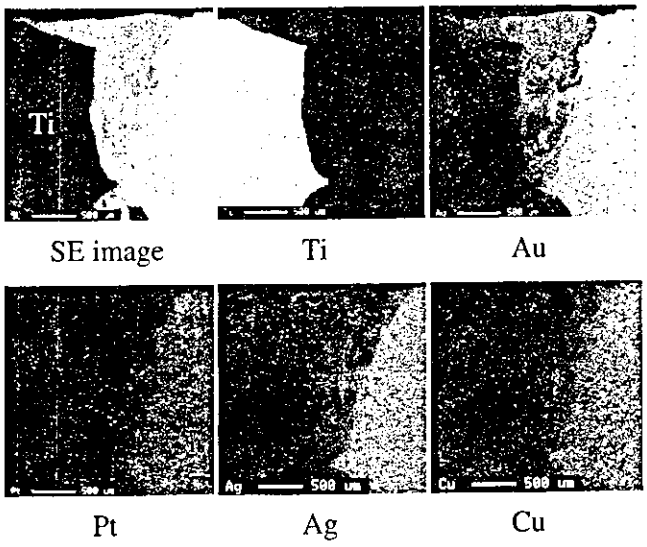

Fig. 4 EPMA elemental mappings of weld zone of titanium (left) and Au-Pt-Ag alloy (right).

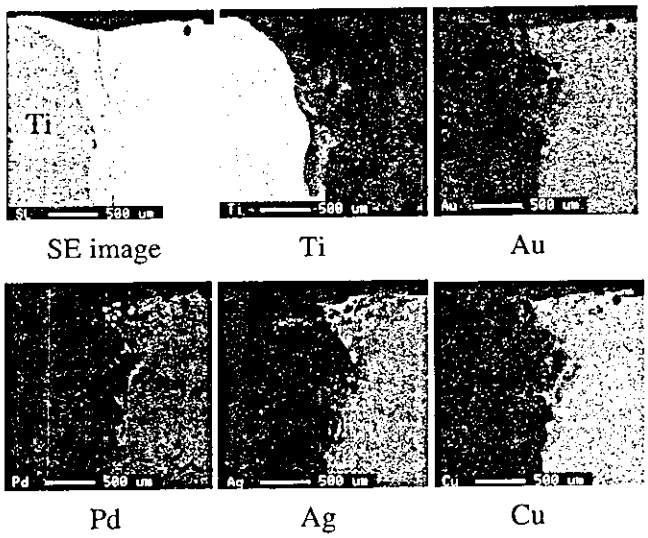

Fig. 5 EPMA elemental mappings of weld zone of titanium (left) and Ag-Pd-Au alloy (right).

of Au-Pt-Ag alloy, Ti and the alloy were soluble in the weld zone, but in some areas the concentration of Ti and the alloy showed the opposite distribution. In the case of Ag-Pd-Au alloy, Ti and the alloy were mutually mixed though the melted zone was not homogeneous. The alloy was relatively soluble in base Ti, while Ti partly melts in the alloy. Ag was uniformly distributed on the Ti side, but there were Ag rich phases with the higher concentration than the alloy.

Fractured surface of welds between the similar metals showing the largest fracture strength was presented in Fig. 6. The melted zones were not extended all over the weld except for Ag-Pd-Au alloy. The fracture surface shows the dimple pattern and porosity. Cup and cone pattern was observed in the fractured surface of the Au-Pd-Ag alloy weld.

Low and high magnification SEM micrographs of the weld fracture surface of Ti and Au-Pt-Ag alloy were shown in Fig. 7.

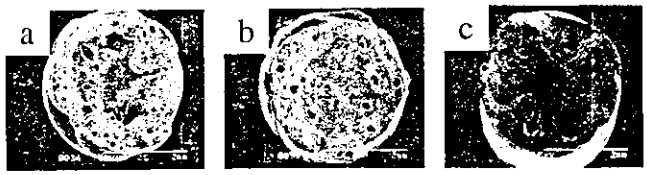

Fig. 6 SEM images of fracture surface of welds of similar metals. a: Au-Pt-Pd alloy b: Ag-Pd-Au alloy c: Titanium.

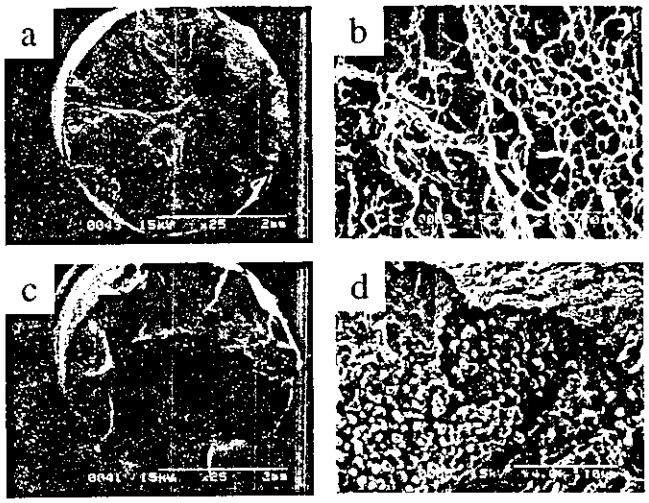

Fig. 7 SEM images of fracture surface of the welds of titanium and Au-Pt-Ag alloy. Maximum fracture strength (a: ×25, b: ×5000). Minimum fracture strength (c: ×25, d: ×4000).

The upper photographs show the fracture surfaces showing the highest welding fracture strength. The melting was extended to the bar core as shown in Fig. 7(a). There were cracks and porosities in the weld. The dimple pattern was observed in Fig. 7(b).

The bottom photographs show the fracture surfaces for the lowest fracture strength. A decrease of the weld zone was observed in Fig. 7(c), due to the alloy under-fill. Porosities and cracks were increased. Different phases of small granular particles were found near the crack in Fig. 7(d).

Figure 8 and Fig. 9 show the mean values and standard deviation of fracture strength of the welds as function of the output current and spot diameter. In both cases, the data for the spot diameters 0.6 mm and 0.9 mm at 300 A output current were omitted because of metal sputtering. The 0.6 mm spot diameter was not adopted for the same reason at 250 A output current. The highest average fracture strength (108.9 MPa) was obtained for Ag-Pd-Au alloy at 200 A and 1.2 mm spot diameter. On the other hand, using Au-Pt-Ag alloy, the highest average fracture strength was 137.2 MPa at 250 A output current and 1.2 mm spot diameter. At lower output current (150 A) the fracture strength decreased (107.4 MPa) for 0.6 mm spot diameter. With the exception of 200 A outputs current no uniform increase in the fracture strength were observed by the variation of the output current and the spot diameter.

Figure 10 presents the welding fracture strength based on the best data for different joint combinations. For the joints made of the similar alloy the welding fracture strength was

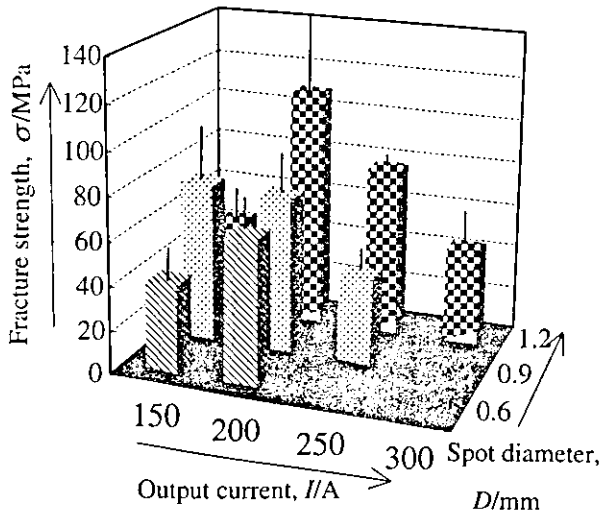

Fig. 8 Fracture strength of welds of titanium and Ag-Pd-Au alloys.

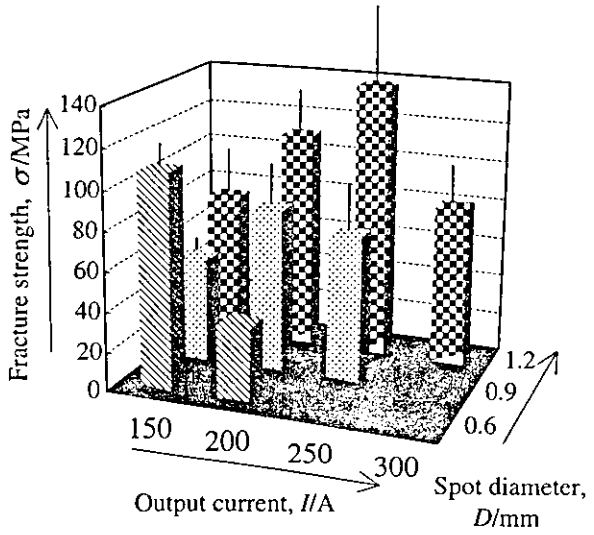

Fig. 9 Fracture strength of welds of titanium and Au-Pt-Ag alloys.

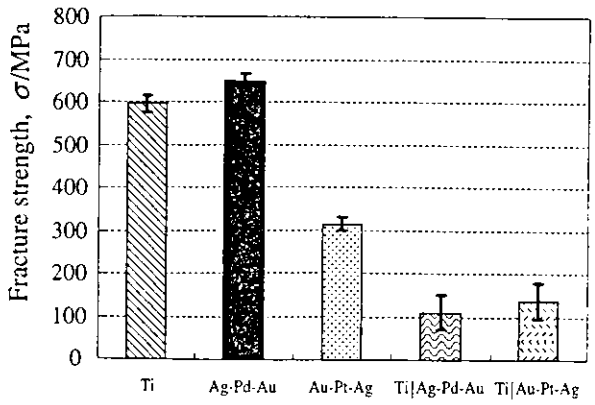

Fig. 10 Comparison of fracture strength of welds of the dissimilar metals with similar metals.

594.9 MPa for Ti, 648.8 MPa for Ag-Pd-Au alloy, and 312.9 MPa for Au-Pt-Ag alloy. The joints of different combinations of Ti and Ag-Pd-Au, Ti and Au-Pt-Ag showed

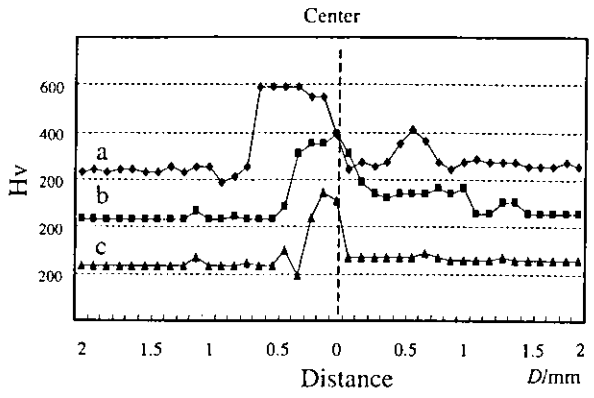

Fig. 11 Vickers hardness of weld zone of titanium and Ag-Pd-Au alloy. a: section edge b: 0.5 mm below c: 1.0 mm below.

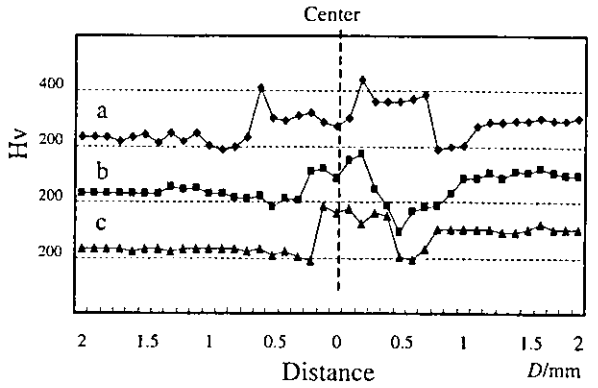

Fig. 12 Vickers hardness of weld zone of titanium and Au-Pt-Ag alloy. a: section edge b: 0.5 mm below c: 1.0 mm below.

the welding fracture strength lower than those of the similar alloy.

Figure 11 and Fig. 12 were the inside the welded zones shown in EPMA mappings of Figs. 4 and 5, respectively. The lines of a, b and c were Vickers hardness corresponding to cross section edge at surface, 0.5 mm below and 1.0 mm below the edge. Both for Ag-Pd-Au and Au-Pt-Ag alloys, the hardness were higher inside the welded zone and lower just out of the welded zone, heat-affected zones compared with base metals. The hardness in the welded zone was more or less uniform and the maximum hardness of welds was higher by 200 than with base metals in Au-Pt-Ag alloy (Fig. 12). In the Ag-Pd-Au alloy, hardness in the center right region was lower than the left region.

4. Discussion

4.1 Parameters affecting on weldability

The operating parameters of laser-welding machine and the physical properties of metal determine the weld strength. The operating parameters of welding machines are: pulse duration, maximum output, irradiation energy, output energy, irradiation frequency and laser spot diameter.[13] The output current, pulse duration, and spot diameter are adjustable for most of the welding machines used in dentistry.

The following physical properties were considered: beam

Table 2 Physical properties of component elements.

Element	Beam absorption ratio	Thermal conductivity ($W \cdot cm^{-1} \cdot deg^{-1}$)	Melting point(°C)
Ti	0.40	0.17	1668
Au	0.03	2.97	1063
Ag	0.03	3.97	961
Pt	0.27	0.72	1769
Pd	0.26	0.72	1552
Cu	0.06	3.95	1083

absorption ratio, thermal conductivity and melting temperature. Metals with high beam absorption ratio and low thermal conductivity are melted at low output energy levels. Slow heat dissipation due to the low thermal conductivity generates the deep penetration. As shown in Table 2, beam absorption ratios, and thermal conductivities present the remarkable difference for different metals. Ti, Pt and Pd have the high beam absorption ratio, and low thermal conductivity, thus the application of low energy laser welding is possible. In contrast Au, Ag and Cu need high laser energy due to their low beam absorption ratio and high thermal conductivity.

It is well known that different impurities, defects, surface roughness and oxide films affect the beam absorption ratio.[14] In the present study all metal specimens were alumina sandblasted and degreased with acetone in order to improve their beam absorption ratio.

4.2 Thermoconductive and keyhole type melting

Laser welding induces either the thermoconductive or keyhole type melting of metal.[15] At low irradiation energy the thermoconductive melting is predominant when penetration depth is small and metal is melted only at the surface. When high-energy laser concentrates the energy of several kW on a small spot, keyhole type melting is produce. During keyhole type melting important quantity of metal is evaporated. The tremendous generated heat combined with the intense metal evaporation generates the deep holes called keyholes, which are rapidly filled with molten metal as the irradiation cease and metal vapor pressure drops. In order to obtain the high weld strength, the perfect melting is needed in the center of weld zones, thus the keyhole type is recommended.

Analyzing the fracture surface of the weld of Ti and Au-Pt-Ag alloy the influence of the spot diameter on the penetration depth was assessed for low output energy. For output of 150 A and spot diameter 1.2 mm thermoconductive type with small penetration depth was observed (Fig. 2). In addition the un-melted regions are visible for output 150 A, spot diameter 0.9 mm, and output 200 A, spot diameter 1.2 mm (Fig. 2). Increasing the output energy and decreasing the spot diameter further, keyhole type predominates. However, molten metal loss caused by metal sputtering under high density beam irradiation generates the weld under-fill, especially at small spot diameters. This atypical under-fill decreases the actual melting area, and affects the weld strength (Fig. 9). Both melting types were also observed in the case of the welding between Ti and Ag-Pd-Au alloy.

4.3 Macrosegregation in the welds of dissimilar metals

Weld of dissimilar metals presents segregation at macroscopic scale called macrosegregation. According to Dr. Shindo,[16] "A very important mechanism for macrosegregation is the convection of the solute-rich interdentritic liquid in the mushy zone of the solidifying ingot. This convection is caused by the gravity force and the shrinkage of the liquid metal during solidification. The dendritic structure in the weld mushy zone is much finer than in the ingot mushy zone. Macrosegregation due to convection in the weld mushy zone would be rather small."

There are important differences between the beam absorption ratio, thermal conductivity and melting point of the used metals, thus their melting behavior is very different. One of the metals melts easily while the other one does not melt properly under the same laser irradiation conditions. The welding pool solidifies before the uniform mixing of metals because of the fast and premature solidification.

Figures 3a, b shows the reflection electron image of the weld zone, evidencing the presence of light and heavy elements due to the macrosegregation. EPMA analysis of the weld of Ti and Ag-Pd-Au alloy indicates that the precious metals are lumped inside the welding pool (Fig. 5), and there is a remarkable heterogeneous distribution of Au, Pd and Ag. Similar heterogeneous precious metal distribution was observed in the weld of Ti and Au-Pt-Ag alloy (Fig. 4). However the elemental distribution was more uniform than in the case of the Ti and Ag-Pd-Au alloy weld. The boundary between the base Ti and the solidified bead is more defined than that between the base precious alloys and the bead (Fig. 3). Ti melts faster than the precious metals due to its high beam absorption ratio and low thermal conductivity, thus the melting alloys distribute heterogeneously in the melted Ti.

4.4 Weld defects

The microscopic observation also showed the defects in the weld. The main weld defects are the crack and the porosity.[17] The cracks are generated during or after welding, and are produced by overheat of the welding zone and the heat affected zone (HAZ). The crack in the weld zone is called solidification cracking and the crack in HAZ liquation crack. The solidification cracking is generated by contraction stress that arises in the welding and often occurs between intermetallic compounds in the welding pool of dissimilar metals. The liquation crack is generated by the contraction stress in the grain boundary of HAZ. At the weld zone of the dissimilar metals investigated, a center solidification cracking was observed (Fig. 3b).

The porosity is caused by the entrapment of bubbles of metal vapor, shielding gas and air in the solidifying metal, or the keyhole closure before it is filled by molten metals at the end of irradiation. Figs. 6(a, b, c) and Figs. 7(a, c) present the investigated welds porosity. Root porosity is also found in the lower weld-zone (Fig. 7c).

4.5 Welding strength

The weld strength is dependent on the laser irradiation parameters such as output energy, pulse duration, and spot diameter. The melting types have strong influence on the

fracture strength, and they are determined by the laser output and spot diameter (Fig. 2, Fig. 6, and Fig. 7). High irradiation energy produced cavities in the under filled regions also affects the weld strength. For the welds of Ti and Au-Pt-Ag alloy, the maximum fracture strength of 137.2 MPa was obtained at the laser output of 250 A and spot diameter of 1.2 mm, when in the keyhole-type welding pool, central non-melted regions and porosity were observed. The minimum fracture strength of 36.8 MPa was obtained at the laser output of 200 A, and the spot diameter of 0.6 mm. Large under-fill and porosity was observed. For the maximum fracture strength welds of Ti and Ag-Pd-Au alloy, the keyhole type melting and non-melted areas were observed. As shown below, due to the more uniform metal distribution and to the less weld cracks and porosity, the fracture strength of Ti and Au-Pt-Ag alloy weld is generally higher then for Ti and Ag-Pd-Au alloy weld.

4.6 Fracture surface and welding strength of similar and dissimilar combination

The maximum fracture strength of the weld between Ti and dental precious alloys is much lower than for the weld of the similar metals (Fig. 10), because of the higher defects occurrence (Fig. 3). The investigated welds between dissimilar metals showed 3 up to 6 times smaller maximum fracture strength then those for similar metals. Only a few weld cracks and little under-fill are observed in the welds of similar metals, although porosity and dimple pattern is present in the ductile fracture. The maximum fracture strength of the weld of similar metals is: 648.8 MPa for Ag-Pd-Au alloy at output 320 A, 312.9 MPa for Au-Pt-Ag alloy at output 300 A, and 594.9 MPa at output 200 A in Ti. Higher output energy is needed to form welding pool in dental precious alloys than in Ti, because of their low beam absorption ratio and high thermal conductivity (Table 2). Among the investigated metals, the Au-Pt-Ag alloy weld had the highest fracture strength, and the weld presents the extended porous structure with numerous non-melted areas (Fig. 6a).

The fractured surface morphology of dissimilar metal welds explains their fracture behavior. Deep penetration along with high porosity and dimple pattern is observed in the ductile fracture for the weld of Ti and Au-Pt-Ag alloy, weld with the highest fracture strength (Figs. 7a, b). Welds with the minimum fracture strength are regularly fractured in the welding pool area.

In this case numerous under-fills, weld cracks, and porosity are observed on the fracture surface (Fig. 7c). In addition, near the crack, intermetallic compound-like granular material was observed (Fig. 7d). It is well known that Ti forms intermetallic compounds with Au, Pt, Pd, Ag and Cu.[18–22] These compounds could lower the weld strength between dissimilar metals.

The comparison between fracture strength in Figs. 8, 9 and observation of fracture surface of welds of Fig. 2 leads to the recognition of the tendency that the region, the conditions for relatively high welding strength situates on the diagonal from the lower left (low output current and small spot diameter) to the upper right (high output current and large spot diameter) of Fig. 2. In the lower right where high output current for small diameter cause too high beam density leading to the volatilization (keyhole type melting). In the upper left where low current for large diameter gives the insufficient beam density which produces the shallow welds (thermoconductive type melting). For both these conditions strength is low the welds are too weak to test.

4.7 Hardness distribution in the welds

The hardness test is an effective evaluation method of the metallurgical changes produced by welding. The hardness of the welding pool is higher by 200 units in the weld of Ti and Au-Pt-Ag alloy, respectively by 400 units in the weld of Ti and Ag-Pd-Au alloy than the hardness of the base metals. The hardness varies continuously along the transversal section of the weld (Fig. 11, Fig. 12). However this variation is less pronounced in the weld of Ti and Au-Pt-Ag alloy than of Ti and Ag-Pd-Au alloy. We suppose that metallurgical changes of the weld zone determine their hardness. The reflection electron images and the elemental mapping images of the welds evidenced the visual differences of the solidification patterns in both welds (Fig. 3, Fig. 4, and Fig. 5). Isolated points of high hardness observed in the welding pool may be produced by different phases of intermetallic compounds of Ti and the precious metals. Near the welding pool the hardness of the base metal is lower then normal, due to heat affected zone.

5. Conclusions

(1) Reflection electron image and EPMA mapping showed the remarkable heterogeneity of the components concerned.

(2) The welding cracks and porosities were observed in microstructures of the welds.

(3) The hardness increased in the weld zone compared with the base metals.

(4) The fracture strength of the dissimilar welds was much lower than that of the similar metals, mainly due to the cracks and pores formed in the weld zones, as a result of insufficient melting and mixture between components with different properties.

(5) The fracture strength in the dissimilar combinations was lower for the laser irradiation conditions to produce the weld of the thermoconductive type at larger diameter with low current which gives the too shallow welds due to the insufficient energy and that of the keyhole type at small diameter with high beam energy which causes the volatilization.

(6) The higher fracture strength was obtained in the intermediate conditions of these above of (5) and the condition for the highest load was situated with the higher current (200 A or 250 A) at large spot diameter (1.2 mm).

Acknowledgements

The authors thank Dr. Yoshinobu Nodasaka, Dr. Iosif D. Rosca, and Mr. Toshi Sugawara, from Hokkaido University, Graduate School of Dental Medicine, for the valuable advices. This study was supported by the 2003 year Grant-in-Aid for Scientific Research No. 15922002 by Japan Society for the Promotion of Science.

REFERENCES

1) T. H. Gordon and D. L. Smith: J. Prosthet Dent. **24** (1970) 472–476.
2) J. D. Preston and M. H. Reisbick: J. Dent. Res. **54** (1975) 232–134.
3) D. L. Smith, A. P. Burnett and T. H. Gordon Jr: J. Dent. Res. **51** (1972) 161–167.
4) G. Sjogren, M. Anderssin and M. Bergman: ACT Odontol. Sacand. **68** (1988) 248–253.
5) D. F. Williams: *Biocompatibility of Clinical Implant Materials*, (CRC Press, Inc Boca Raton, Florida, 1984) pp. 7–44.
6) J. Shimada: The J. Jap. Soc. Dent. Mat. Dev. **10** (1987) 362–375.
7) A. C. Louly, F. Mora, B. K. Moore, C. J. Andres and C. J. Goodacre: The Int. J. Prosthod. **4** (1991) 425–431.
8) G. Byrne, L. W. Laub, J. Y. Hu and M. F. Land: J. Prosthet. Dent. **68** (1992) 591–596.
9) T. Yamagishi, M. Ito and Y. Fujimura: J. Prosthet. Dent. **70** (1993) 264–273.
10) R. R. Wang and G. E. Welsch: J. Proshet. Dent. **74** (1995) 421–530.
11) G. Sjogren, M. Andersson and M. Bergman: Acta Odontol. Scand. **46** (1988) 247–253.
12) B. Einar, W. C. Wagner, G. Davik and E. R. Dootz: J. Proshet. Dent. **74** (1995) 250–257.
13) T. Shinosaki and T. Togaya: Quint. Dent. Tech. **24** (1999) 43.
14) T. Shinosaki and T. Togaya: Quint. Dent. Tech., Extra issue, (2002) 199–208.
15) T. Shinosaki and T. Togaya: Quint. Dent. Tech., Extra issue, (2002) 199–208.
16) K. Shindo: *Welding Metallurgy*, (John Wiley & Sons New York, U.S.A, 1987) pp. 204–206.
17) K. Nishimoto: Journal of the japan welding society. **68** (1999) 20–27.
18) M. Hansen and K. Anderko: *Constitution of Binary Alloys*, (McGraw-Hill Book Company New York, Toronto, London, 1958) pp. 59–59.
19) M. Hansen and K. Anderko: *Constitution of Binary Alloys*, (McGraw-Hill Book Company New York, Toronto, London, 1958) pp. 238–238.
20) M. Hansen and K. Anderko: *Constitution of Binary Alloys*, (McGraw-Hill Book Company New York, Toronto, London, 1958) pp. 643–643.
21) M. Hansen and K. Anderko: *Constitution of Binary Alloys*, (McGraw-Hill Book Company New York, Toronto, London, 1958) pp. 1128–1128.
22) M. Hansen and K. Anderko: *Constitution of Binary Alloys*, (McGraw-Hill Book Company New York, Toronto, London, 1958) pp. 1143–1143.

Dental Materials Journal 23(4) : 593−599, 2004

Distortion of Laser Welded Titanium Plates

Keiji IWASAKI[1], Shoji OHKAWA[1], Iosif D. ROSCA[2], Motohiro UO[1], Tsukasa AKASAKA[1] and Fumio WATARI[1]

[1]Biomedical, Dental Materials and Engineering, Division of Oral Health Science, Course of Oral Medical Science, Graduate School of Dental Medicine, Hokkaido University, Kita 13 Nishi 7, Kita-ku, Sapporo, 060-8586, Japan

[2]Department of Polymer Chemistry and Technology, Faculty of Industrial Chemistry, Polytechnic University of Bucharest, 149 Calea Victoriei, Sector 1, 71101, Romania

Corresponding author, E-mail:keiji-iwasaki@nifty.com

Received July 21, 2004/Accepted October 28, 2004

The distortion of laser welded titanium plates was assessed for different operating conditions of the laser welding device, and with different welding parameters (in terms of weld point and prewelding). In this study, Nd : YAG laser welding device was used to join the titanium plates. The results showed that distortion increased stepwise after each welding point along the welding zone (one-side welding), but decreased consecutively as the welding proceeded on the second side of the weld (two-side welding). In the case of one-side welding, the dependence of distortion on current and spot diameter presented maxima − due to changes in the welding pool characteristics. For two-side weld the same parameters exercised little influence on its distortion recovery, due to the effect of solidified weld pools from the first side. Current and spot diameter determined the weld pool, which in turn regulated distortion based on shrinkage. Four-point prewelding significantly decreased the final distortion for both one- and two-side welds. Alternating two-side welding of prewelded assembly showed lower distortion than a classic two-side weld.

Key words: Distortion, Laser welding, Titanium

INTRODUCTION

Laser welding is often used to join metal prosthetic appliances[1−6] because it is a simple and fast process. Moreover, it has numerous advantages[7]. Base metals are only slightly affected by the heat effect considering the small welding area. The flow of inert gas prevents base metals from oxidizing. Laser welding exhibits higher joint strength than soldering, and local corrosion is eliminated due to the absence of solder. Defects are easily repaired using filler metals. Proper adjustment of the laser operating parameters − current, pulse duration, and spot diameter − results in good-quality welds.

Titanium and Co-Cr alloy, which own high beam absorption and low thermal conductivity, are suitable for laser welding[8]. Due to its high corrosive resistance and good biocompatibility[9], titanium is a high-value dental metal which is often used as cast or wrought material. Soldering titanium in the presence of flux is difficult due to its increased reactivity at high temperatures[10−14]. Infrared soldering of titanium in argon atmosphere with solder as Ti-Cu-Ni alloy eliminates the inconvenience of using flux[15,16]. Indeed, many soldering inconveniences have been overcome by laser welding.

The pool, strength, and microstructure of laser welds have been extensively investigated, and the effects of different operating parameters have been determined[17−19]. The parameters influence the weld pool, which in turn has a strong influence on weld strength. Distortion, which affects weld performance, is well-known and well-studied in industrial welding[20−22]. Distortion results chiefly from solidification shrinkage and thermal shrinkage during welding. In dental laser welding, distortion affects the joined metal prosthetic appliance such that it does not fit the prepared teeth. Only a few experimental results are available concerning the distortion of titanium prosthetic appliances joined by laser welding[8]. In this study, we investigated the distortion of laser welded titanium plates, and its dependence on the main operating parameters.

MATERIALS AND METHODS

Preparation of titanium plates

Wrought titanium plates (JIS. 2) were accurately processed on a lathe to 1.5-mm thickness, 6.0-mm width, and 30-mm length. The length of the plate was similar to long span bridges of large prosthetic appliances. The plate width was chosen in order to accommodate 10 weld points of 1.0-mm diameter with 50% overlap. Considering the laser welding unit's performance, 1.5-mm thickness was selected to allow two opposite-side welding pools to overlap.

Weld surfaces were sandblasted with 50-micron alumina under 0.2 MPa pressure. Then the plates were cleaned ultrasonically − first in detergent solution, next in pure water, and finally degreased with acetone.

Laser welding unit

The Nd :YAG pulsed laser unit (TANAKA Laser TLL7000 PULS, ATD JAPAN, Tokyo, Japan) was used for welding in argon atmosphere.

Design of stainless steel holder for the titanium plates

Fig. 1 shows the stainless steel holder for a pair of titanium plates. The plates fit in the groove of 1.4-mm depth and 6.0-mm width, located on the upper surface of the holder (Fig. 1-a). The two titanium plates were placed in the groove with their weld surfaces in firm contact. A stainless steel plate (Fig. 1-b) was used to fasten one of the plates. The other plate remained free to move vertically. Laser was properly focused on the weld zone by moving the stand with the holder on it until the two guide beams were superposed.

Distortion measurement of a classically welded assembly

1. One-side welding

Two titanium plates were placed in the holder as mentioned above. The weld consisted of 10 welding points starting from the middle of the weld and continuing toward the edges of the plate, alternating on each side, as shown in Fig. 2. Due to contraction during welding, the opposite edge of free plate rose. The distance between the groove bottom and the lower edge of the risen plate was measured by a micro-digital scope (VH-6300, KEYENCE Co., Tokyo, Japan) with accuracy of ±0.01 mm as shown in Fig. 3. This distance was defined as distortion of the welded assembly. Each final value was averaged over five measurements. The distortion was measured after irradiating each welding point.

The dependence of distortion on laser current and spot diameter was investigated. The laser current varied from 140 A to 230 A at spot diameter of 0.9 mm and pulse duration of 10 ms. As for the spot diameter, it varied from 0.3 mm to 1.2 mm at constant current of 180 A and pulse duration of 10 ms.

2. Two-side welding

After welding was completed on the first side, the assembly was flipped over and the second side was freehand welded. After each point, the assembly was flipped again and fixed in the holder as for one-side welding, and the distortion measured.

Distortion measurement of prewelded assembly

1. Four-point prewelding

Two titanium plates were placed in the holder as for one-side welding. The first welding point was located at 2 mm from the plate edge. The second was preformed in the same position as the first, but after flipping the assembly. The third point was preformed symmetrically to the second point, and the fourth point was preformed in the same position as the third but again after flipping the assembly. The laser output of 140 A was sufficient to produce a keyhole-type welding pool; the pulse duration was 10 ms and the spot diameter was 0.9 mm. The final distortion was measured as described above. The experiments were done in quintuplets.

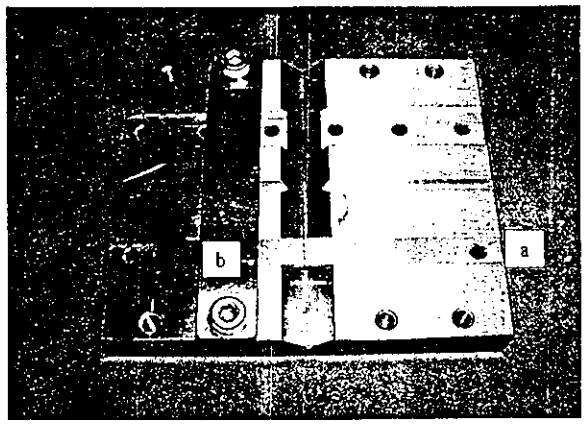

Fig. 1 The stainless steel holder.
a Groove
b Tightening plate

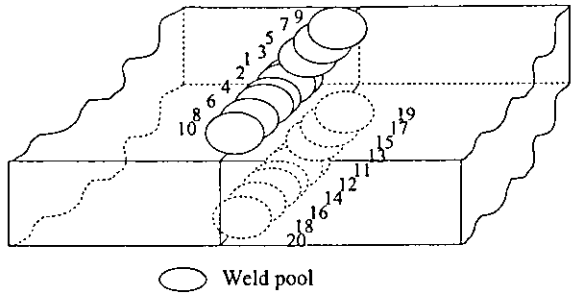

Fig. 2 Weld point order in one-side and two-side welding.

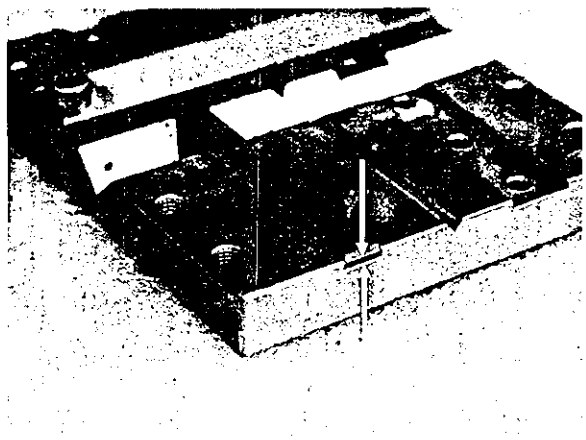

Fig. 3 Measurement of distortion of welded assemblies.

2. Welding of prewelded assembly

The prewelded assembly was fixed in the holder. Afterwards, one- and two-side welding were performed as described previously. Corresponding distortions were measured and averaged over five measurements. The laser current was 200 A, the pulse duration 10 ms, and the spot diameter was 0.9 mm. The reason for selecting high current was that for one-side welding, distortion increased as the current increased (Fig. 7). Thus, if prewelding could reduce distortion at high current, it would accordingly be more effective at other current outputs.

3. Alternating two-side welding

Two-side welding was performed alternately according to the point order shown in Fig. 4. Distortion was measured after each point was irradiated (as described previously). The laser current was 200 A, the pulse duration 10 ms, and the spot diameter was 0.9 mm. The welding parameters were selected for the same reason as mentioned above. All experiments were done in quintuplets. The alternating two-side weld was realized in two different welding conditions: (1) after four-point prewelding, the points on the upper side of Fig. 4 (Point No. 1, 3, 5, 7, 9, 11, 13, 15, 17, 19) were performed with one plate fixed in the holder, and the rest of the points were done freehand; (2) same conditions as described for welding condition (1), but without prewelding.

Observation of fractured section of two-side weld

Two-side welds produced at different currents and spot diameters were fractured by tensile force on a mechanical testing machine (Model 4204, Instron Japan, Kawasaki, Japan), and the fractured surfaces were examined by SEM (S-2380N, Hitachi, Tokyo, Japan).

Distortion recovery ratio

The distortion recovery ratio (R) was defined by the following formula:

$$R=\frac{x-y}{x}\times 100\%$$

where x was the distortion at the final 10 points for one-side weld, and y was the distortion of each point for the two-side weld.

RESULTS AND DISCUSSION

We defined incremental distortion as the distortion measured after irradiating each welding point, and final distortion as the distortion measured after completing one-side or two-side welding.

Fig. 5 shows the evolution of incremental distortion for two-side welding at the current of 180 A, pulse duration of 10 ms and spot diameter of 0.9 mm. During welding, distortion increased for the first side and decreased for the second side in a linear fashion. The final distortion after completing the first side of the two-side weld was 0.94 ± 0.09 mm, and that after completing the second side was 0.07 ± 0.06 mm. Solidification shrinkage and thermal shrinkage added up after each welding point, resulting in a stepwise increase of distortion for the one-side welding. Continuing with the second side, shrinkage forces produced by the new welding pools acted in an opposite direction, hence reducing the distortion obtained during one-side welding.

Fig. 6 presents the recovery ratio of incremental distortion during the welding of the second side. Re-

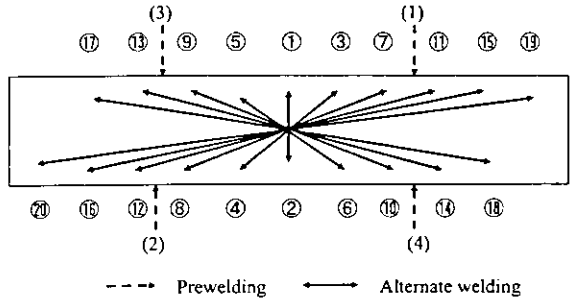

Fig. 4 Weld point order for the alternating two-side welding.

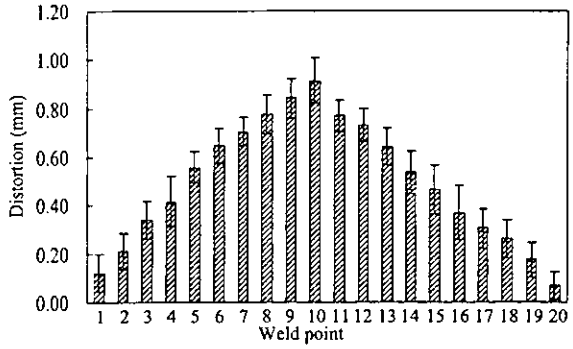

Fig. 5 Incremental distortion for two-side welding (Current 180 A, Pulse duration 10 ms, Spot diameter 0.9 mm).

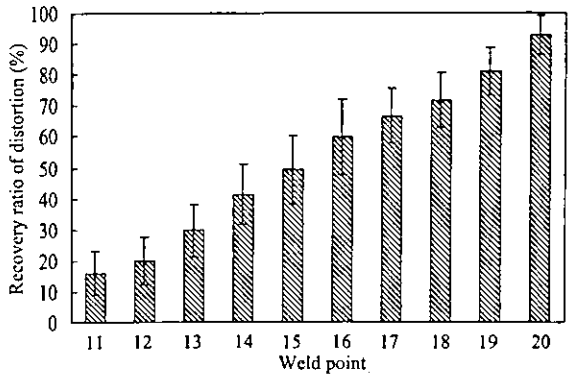

Fig. 6 Recovery of the incremental distortion for two-side welding.

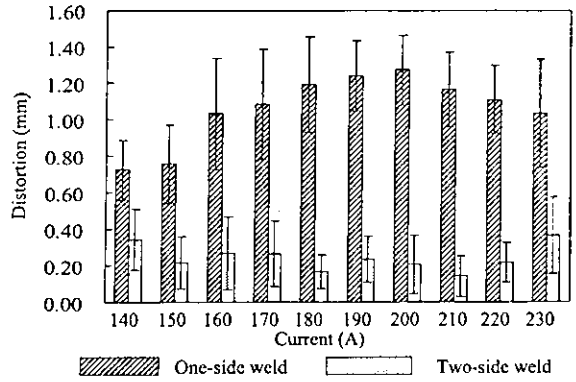

Fig. 7 Effect of current on final distortion.

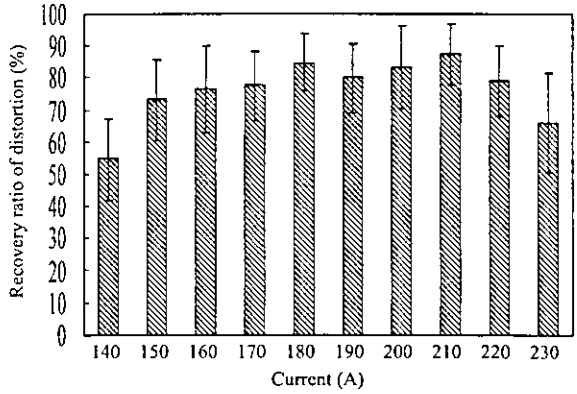

Fig. 8 Recovery of the final distortion for different currents.

covery of the final distortion was $92.77 \pm 6.19\%$. Thus, symmetrical two-side welding was recommended for reducing distortion. Our results showed that recovery of 100% was not attainable if the welding points on the second side were realized in the same welding conditions as for the first side, because the solidified welds on the first side would restrict the shrinkage on the second side.

Effect of current

Fig. 7 shows the influence of current on the final distortion of one-side and two-side welds at pulse duration of 10 ms and spot diameter of 0.9 mm. For the one-side weld, the final distortion presented a maximum of 1.27 ± 0.19 mm at 200 A. As the current increased, the penetration depth increased and distortion increased consequently. Increasing the current further (>210 A), the penetration depth gradually equaled the plate thickness, thus generating meltdown and porosity in the welding pool. As the volume of welding pool decreased substantially, distortion also decreased because of less shrinkage.

Distortion at 180A shown in Fig. 7 is different from that of the 10^{th} weld point in Fig. 5, because the former was the final distortion after 10 irradiations, and the latter was the distortion after each irradiation. We found that the distortion after continuous irradiation was larger than that after each irradiation.

Fig. 8 shows the recovery of the final distortion for different currents. It can be observed that the recovery ratio varied with the current. Recovery was lower at small currents due to the smaller welding pool volume. At high currents, the recovery was also low because laser was able to penetrate through plate and normal welding pools were not formed. Higher recovery was attained in assemblies with large distortion in the one-side welding, meaning that the welding conditions which caused increased distortion also yielded large shrinkage in the two-side welding.

Fig. 9 presents the SEM images of the fractured section of the two-side weld for different currents. Melting depth increased as the current increased. At 140 A, the melting depth was insufficient to recover the distortion. But at higher outputs, the volume of the weld pool increased, thus more significant shrinkage and higher recovery were observed.

Effect of spot diameter

Fig. 10 shows the effect of spot diameter on the final distortion of one-side and two-side welds at the current of 180 A and pulse duration of 10 ms. For the one-side weld, the distortion showed a maximum of 1.17 ± 0.06 mm at the spot diameter of 0.8 mm.

The energy density of laser depends on the spot diameter: the smaller the diameter, the higher the energy density. In the case of small spot diameter, the usual welding pool was not formed due to meltdown and sputter – hence the distortion was smaller. For large spot diameter, the laser had insufficient energy to penetrate through depth, so the distortion was also small.

Fig. 11 shows the recovery of the final distortion for different spot diameters for the two-side weld. The recovery of the final distortion ranged from $53.4 \pm 4.42\%$ to $76.3 \pm 5.64\%$. This recovery ratio was smaller than the case when current output was a changing variable.

Fig. 12 shows the SEM photographs of the fractured section of the two-side weld for different spot diameters. Due to the high energy density for the smallest spot diameter (0.3 mm), the laser penetrated throughout the plate and produced holes and sputter. At the spot diameter of 0.6 mm, pores and sputter were generated by the still-high energy density. The maximum distortion for the one-side weld was obtained at the spot diameter of 0.8 mm when full melting and only a few defects were observed. At the spot diameter of 1.2 mm, the lower energy density kept the middle region of the weld unmelted (Fig. 12(d)), thus the smallest distortion was

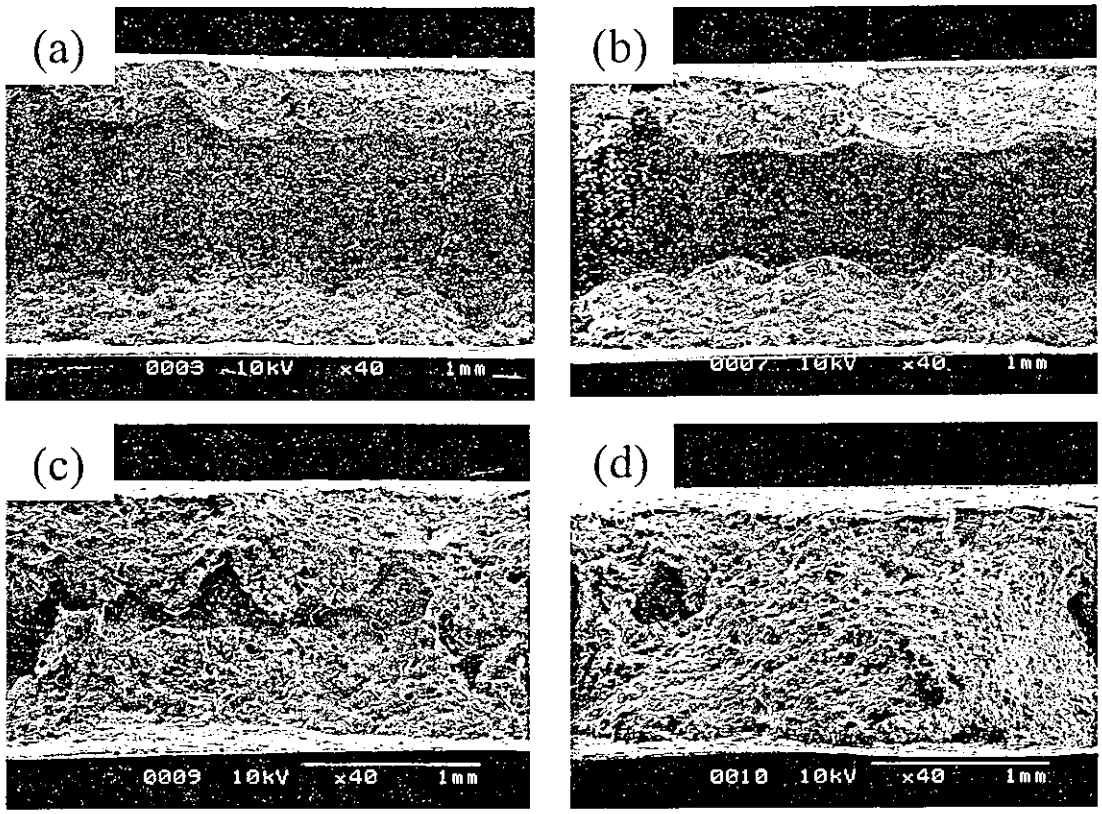

Fig. 9 SEM images of the fractured section of the two-side weld produced at different currents.
(a) Current 140 A, Pulse duration 10 ms, Spot diameter 0.9 mm
(b) Current 150 A, Pulse duration 10 ms, Spot diameter 0.9 mm
(c) Current 160 A, Pulse duration 10 ms, Spot diameter 0.9 mm
(d) Current 170 A, Pulse duration 10 ms, Spot diameter 0.9 mm

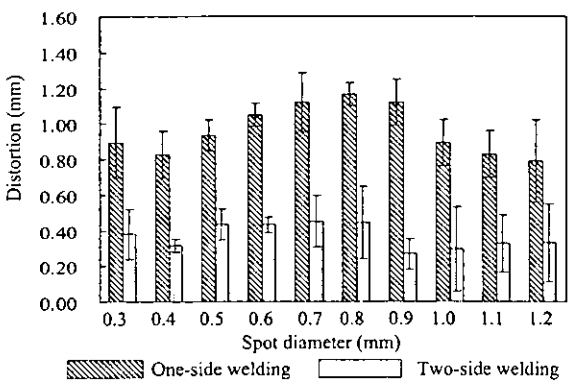

Fig. 10 Effect of spot diameter on final distortion.

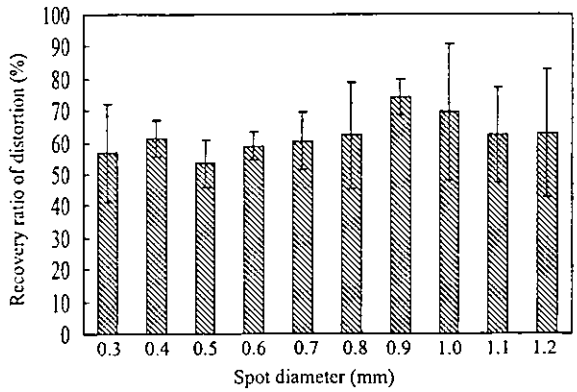

Fig. 11 Recovery of the final distortion for different spot diameters.

observed. Based on the results of this study, the size of spot diameter had strong influence on the volume of the weld pool, which then affected the shrinkage forces.

Effect of prewelding

Fig. 13 shows the effect of prewelding on the final distortion of one-side and two-side welds. As prewelding was executed symmetrically in only four points at low laser output, the corresponding final distortion was small. After prewelding, the assembly

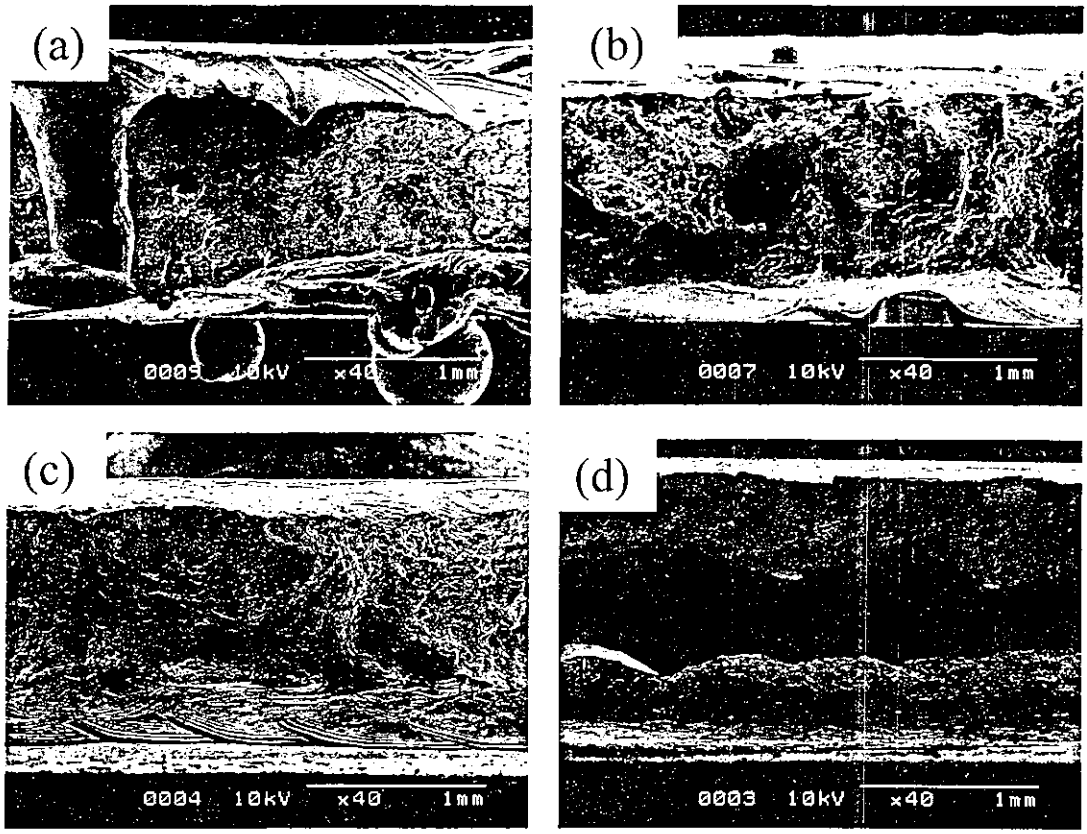

Fig. 12 SEM images of the fractured section of the two-side weld produced at different spot diameters.
(a) Current 180 A, Pulse duration 10 ms, Spot diameter 0.3 mm
(b) Current 180 A, Pulse duration 10 ms, Spot diameter 0.6 mm
(c) Current 180 A, Pulse duration 10 ms, Spot diameter 0.8 mm
(d) Current 180 A, Pulse duration 10 ms, Spot diameter 1.2 mm

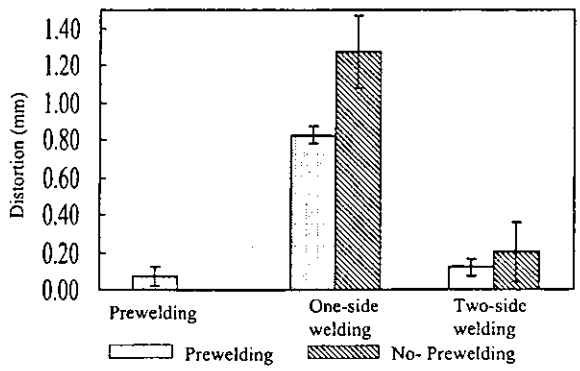

Fig. 13 Effect of prewelding on final distortion.

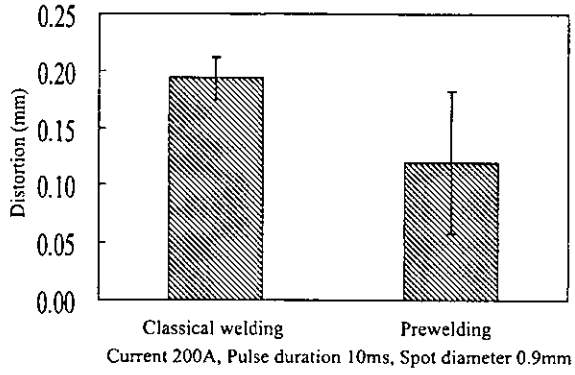

Fig. 14 Final distortion of the alternating two-side welding for two conditions.

became more stable during the final welding. For the one-side weld, the final distortion of the prewelded assembly was 0.83 ± 0.05 mm and that of the classical weld was 1.27 ± 0.19 mm – which was 35.11% larger than the prewelded assembly. Similar result was obtained for the two-side weld.

After prewelding, shrinkage of the first welding point was reduced by the previous four prewelding points. Further, the subsequent welding points were expected to show smaller and smaller shrinkage as the previous welding points strengthened the assembly. We believe that prewelding conditions should be selected such that the prewelded assembly would present small distortion and good welding strength.

Based on the results of this study, prewelding was a useful and simple technique that reduced the final distortion of the laser welded prosthetic appliances.

Distortion of the alternating two-side welding

Fig. 14 shows the final distortion of the alternating two-side welding for two different welding conditions. Using prewelding, the final distortion was significantly reduced compared to the classical alternating two-side welding. Besides decrease in distortion by prewelding, the alternating welding points executed on the diagonal line would further contribute to a smaller distortion.

CONCLUSIONS

Distortion of laser welded titanium was investigated under various operating conditions, and methods for reducing the final distortion were identified as follows.

1. Two-side welding showed small distortion compared to one-side welding.
2. Four-point prewelding significantly reduced distortion by stabilizing the welding assembly.
3. Alternating two-side welding resulted in the smallest distortion.
4. Current and spot diameter had strong influence on one-side welds.

ACKNOWLEDGEMENTS

The authors wish to thank Dr. Yoshinobu Nodasaka and Mr. Toshi Sugawara, from Hokkaido University, Graduate School of Dental Medicine, for their invaluable advice. This study was supported by the Year 2004 Grant-in-Aid for Scientific Research, No 16922210, of the Japan Society for Promotion of Science.

REFERENCES

1) Gordon TH, Smith DL. Laser welding of prostheses — An initial report. J Prosthet Dent 1970; 24: 472-476.
2) Sjögren G, Anderson M, Bergman M. Laser welding of titanium in dentistry. Acta Odontol Scand 1988; 68: 248-253.
3) Preston JD, Reisbick MH. Laser fusion of selected dental casting alloys. J Dent Res 1975; 54: 232-234.
4) Smith DL, Burnett AP, Gordon Jr TE. Laser welding of gold alloys. J Dent Res 1972; 51: 161-167.
5) Yamagishi T, Ito M, Fujimura Y. Mechanical properties of laser welds of titanium in dentistry by pulsed Nd:YAG laser apparatus. J Prosthet Dent 1993; 70: 264-273.
6) Fujioka S, Kakimoto K, Inoue T, Okazaki J, Komasa Y. Metallurgical effects on titanium by laser welding on dental stone. Dent Mater J 2003; 22: 581-591.
7) Shinosaki T, Togaya N. The dental technology of the titanium. Part 2: Present status of dental laser welding in Japan. Quint Dent Tech 2002; Extra Issue: 199-208.
8) Lee WS. The actions of the titanium by the beam on laser welding. Quint Dent Tech 2002; Extra Issue: 209-218.
9) Williams DF. Biocompatibility of clinical implant materials, CRC Press, Inc Boca Raton, Florida, 1984, pp.7-44.
10) Kikuchi H, Ling S, Yuda M, Matsudaira S, Nishiyama M. Soldering of titanium. Part 1. Composition of commercial titanium solder and tensile soldering strength. J J Dent Mater 1995; 14: 213-218.
11) Shimada J. A soldering of titanium and titanium alloys with IR soldering equipment. J J Dent Mater 1987; 10: 362-375.
12) Togaya T, Yabugami M, Tani Y. Brazing of titanium. The J Dent Med (Japan) 1989; 30: 399-407.
13) Miura I, Sakurai M. Study on dental titanium and zirconium alloys. Part VI: Brazing alloys and fluxes for titanium. Reports of Institute for Medical and Dental Engineering, Tokyo Med Dent Univ 1956; 1: 34-40.
14) Ohkawa S, Kondo S, Hanawa T, Sugawara T, Watari F. KHF2-LiF-NaCl-KCl fluxes for the brazing of titanium. J J Dent Mater 1994; 13: 501-508.
15) Byrne G, Laub LW, Hu JY, Land MF. The fit of fixed partial dentures joined by infrared soldering. J Prosthet Dent 1992; 68: 591-596.
16) Wang RR, Welsch GE. Joining titanium materials with tungsten inert gas welding, laser welding and infrared brazing. J Prosthet Dent 1995; 74: 421-530.
17) Einar B, Wagner WC, Davik G, Dootz ER. Mechanical properties of laser-welded cast and wrought titanium. J Prosthet Dent 1995; 74: 250-257.
18) Won DH, Bae TS, Ohkawa S, Watari F. The influence of current on the tensile strength of laser-weld titanium joints. Metals and Materials International 2003; 9: 493-496.
19) Liu J, Watanabe I, Yoshida K, Atuta M. Joint strength of laser-welded titanium. Dental Materials 2002; 18: 143-148.
20) Masubuchi K. Metals handbook, 9th ed, ASM, Ohio, 1983, pp.869-881.
21) Kou S. Welding metallurgy, John Wiley & Sons, New York, 1987, pp.109-115.
22) Suzuki H. Recent welding engineering, Corona Publishing Co., Tokyo, Japan, 1975, pp.191-203.

Materials Transactions, Vol. 45, No. 4 (2004) pp. 1132 to 1139
Special Issue on Frontiers of Smart Biomaterials
©2004 The Japan Institute of Metals

Slip Casting of Titanium Powder for Dental Prosthetic Appliances

Shoji Ohkawa[1], Kuniyoshi Ishii[2], Motohiro Uo[1], Toshi Sugawara[1] and Fumio Watari[1]

[1]*Department of Oral Health Science, Division of Dental Materials and Engineering, Graduate School of Dental Medicine, Hokkaido University, Sapporo 060-8586, Japan*
[2]*Department of Materials Engineering, Division of Materials Science and Engineering, Graduate School of Engineering, Hokkaido University, Sapporo 060-8628, Japan*

The feasibility of using slip casting of titanium powder as a method for manufacturing dental prosthetic appliances was examined. Slips with water-powder (W/P) ratios, 0.318, 0.354 and 0.391, and with minimum viscosities were cast in plaster molds. Castings were sintered in an argon atmosphere at 1373, 1473 and 1573 K for 3.6, 7.2 and 10.8 ks, respectively. Green densities and strengths of castings were 2.20 kg/m^3 and 2.31–3.82 MPa, respectively. Linear shrinkages and relative densities of sintered castings varied from 17.6 to 20.8% and 0.82 to 0.97 of the theoretical density of titanium, respectively. Tensile strengths and Vickars hardness of the sintered castings were 199.5–315.4 MPa and 233.0–247.7, respectively. There was almost no elongation. Decreasing porosity and crystal grain growth were found in the microstructures of sintered castings and rod-like precipitates of TiC with α-titanium were also observed. Concentrations of carbon and oxygen in the microstructures of sintered castings were higher than those in wrought titanium. Fractured surfaces showed ridge patterns typical of brittle fracture. Further modification of the sintering atmosphere and the additives for the slip is needed to improve the microstructure of slip-cast sintered titanium.

(Received November 6, 2003; Accepted March 15, 2004)

Keywords: *titanium, slip casting, viscosity, sintering, dental materials*

1. Introduction

Titanium is an attractive biomaterial because of its good biocompatibity.[1)] In dentistry titanium is processed by machining and casting. Ready-made artificial tooth roots are produced using wrought titanium.[2)] Recently CAD/CAM design is also used to make crowns and bridges of titanium.[3–5)] But up to now there are only a few CAD/CAM applications because of the sophisticated machinery involved and higher costs. The development of titanium casting reached higher level of refinement than that of CAD/CA design, because of the long history of the conventional dental lost wax process.[6–10)] Titanium prosthetic appliances for individual use such as crowns, bridges, dentures and superstructures of implants can be made by casting.[11)] However the dental casting of titanium presents a few inconvenients:[12)] (1) the hard α-case on surface of cast titanium decreases the metal ductility and fatigue resistance; the removal of the α-case affects the fitting of the cast to prepared teeth; (2) incomplete casting often occurs because of the low mold permeability and inadequate gas pressure in the casting machine; (3) low pressure in the casting machine promotes the internal porosity; (4) usually special expensive casting machines are necessary.

Powder metallurgy (P/M) represents a solution for a part of the problems in the dental casting of titanium. Metallic materials are not melted and the investment materials are not used in the process. The formation of α-case is decreased. P/M products have net-shapes and incomplete casting is not encountered. The porosity of the products is controlled by adjusting the forming and the sintering conditions. There have been some basic studies on application of powder metallurgy to dentistry. Oda[13)] studied various properties of sintered titanium and a titanium alloy, using pressure forming with a metal die as a forming method of powders. He reported that sintered materials of Ti-Al-Cu powder mixtures were more desirable than sintered pure titanium for dental appliances. He also described his techniques for forming powders in order to produce forms of appliances for clinical use such as a single crown, a single crown attached to a clasp and a denture base. Lee[14)] carried out a study on titanium sintered by a plasma-activated sintering method based on the idea that practical forms of the various appliances could be manufactured by wire electric discharge machining of blocks sintered in short times by plasma-activated sintering method. Fuys *et al.*[15)] examined the physical properties of a nickel-base alloy and a partial denture casting alloy, fabricated by isostatic pressing and sintering, and they concluded that the physical properties of the sintered materials are comparable with those of the cast alloy and compact bone.

Using powder metallurgy in dentistry one of the most important process before sintering is the forming of the prosthetic appliances from powder. In the studies cited above, the pressure forming is done using a metal mold, graphite mold and rubber mold. Dental prosthetic appliances are mostly personalized. Slip casting is suitable as forming method of the prosthetic appliances from powder. Slip casting is often used in ceramics and powder metallurgy.[16–18)] The slip is a mixture of metal powder, water and additives. The slip is poured into a porous plaster mold and left standing while water is absorbed into the mold. Then the casting is separated from the mold, dried, and sintered.

We intend to use the conventional dental lost wax process for producing molds for slip casting. Various sizes and forms of dental wax patterns can be prepared by melting and carving in order to fit a large variety of the prostheses. Removing the wax through melting and burning produces the cavities in the molds. The mold is filled with the slip at room temperature under centrifugal force. After water absorption and drying the casting is sintered in the mold. We expect that the sintering shrinkage is compensated by using high-expansive molds.

The purpose of the present study was to assess the potential of slip casting of titanium powder, and to determine the